

University of Alberta

**Thermally Induced Fibre Deformation Using a
High Frequency Magnetic Field**

by

Yuhui Shang



A thesis submitted to the Faculty of Graduate Studies and Research in partial
fulfillment of the

requirements for Master of Science

Department of Mechanical Engineering

Edmonton, Alberta
Fall 2004



Library and
Archives Canada

Bibliothèque et
Archives Canada

Published Heritage
Branch

Direction du
Patrimoine de l'édition

395 Wellington Street
Ottawa ON K1A 0N4
Canada

395, rue Wellington
Ottawa ON K1A 0N4
Canada

Your file *Votre référence*

ISBN: 0-612-95851-5

Our file *Notre référence*

ISBN: 0-612-95851-5

The author has granted a non-exclusive license allowing the Library and Archives Canada to reproduce, loan, distribute or sell copies of this thesis in microform, paper or electronic formats.

L'auteur a accordé une licence non exclusive permettant à la Bibliothèque et Archives Canada de reproduire, prêter, distribuer ou vendre des copies de cette thèse sous la forme de microfiche/film, de reproduction sur papier ou sur format électronique.

The author retains ownership of the copyright in this thesis. Neither the thesis nor substantial extracts from it may be printed or otherwise reproduced without the author's permission.

L'auteur conserve la propriété du droit d'auteur qui protège cette thèse. Ni la thèse ni des extraits substantiels de celle-ci ne doivent être imprimés ou autrement reproduits sans son autorisation.

In compliance with the Canadian Privacy Act some supporting forms may have been removed from this thesis.

Conformément à la loi canadienne sur la protection de la vie privée, quelques formulaires secondaires ont été enlevés de cette thèse.

While these forms may be included in the document page count, their removal does not represent any loss of content from the thesis.

Bien que ces formulaires aient inclus dans la pagination, il n'y aura aucun contenu manquant.

Canada

Acknowledgements

There are lots of people I would like to thank for a huge variety of reasons.

I specifically wish to thank my advisor, Dr. Walied Moussa and Dr. Warren Finlay, for their endless support in my research and life at the University of Alberta. I could not have imagined having better advisors and mentors for my M. Sc. Particularly, thank them for putting up with my awkward in English and keeping pushing me forward. I wish to acknowledge the support of my friends at the multiphysics and MEMS computation lab, and Dr. Walied Moussa and Dr. Warren Finlay's research group at University of Alberta. I would also like to thank Dr. Tsui, Ying for the discussion on the related theories. The professors and researchers at this school have always made the time to answer questions and work through problems together. I am honored to have worked with such bold and intellectual people.

Finally, I would have not done this without the continued love of my family, parents, and friends.

Contents

Chapter 1: Overview.....	1
1.1 Introduction.....	1
1.2 Background.....	1
1.3 Sources of Field Energy.....	3
1.4 Comparing of Field Energies.....	5
1.5 Bio-effects of Electromagnetic Tissue Interaction.....	10
1.6 Experiments and Clinical applications of Magnetic Field and Ferro- magnetic Materials.....	15
Chapter 2: The Electromagnetic Field Energy Deposition.....	23
2.1 Basic Concept of Magnetic Materials and Magnetic Field	23
2.2 B-H curve and Hysteresis Losses.....	26
2.3 Néel Relaxation Losses.....	30
2.4 Brownian Relaxation Losses.....	32
2.5 Eddy Current Losses.....	34
2.6 Comparing of Heat Capacity of Various Mechanism.....	39
2.7 Energy, Thermal and Solid Modeling.....	41
Chapter 3: FEM Multiphysics model.....	46
3.1 Coupled Electromagnetic-thermal Analysis.....	46
3.2 Model Overview	50
3.3 Material Properties.....	52
Chapter 4: FEM Simulation.....	57

4.1	2-D modeling.....	57
4.2	3-D modeling.....	64
Chapter 5: Parametric Study.....		69
Chapter 6: Conclusion and Future work		73
Reference:.....		76

List of Tables:

Table 1-1	List of available field energy resources and governing equations.....	6
Table 2-1	The list of magnetic field flux density.....	24
Table 2-2	List of Ferro energy deposition experiment data.....	30
Table 3-1	Material properties.....	52
Table 4-1	Energy depositions rate of the tissues Units: W , W / m^3	60
Table 5-1	Energy deposition at different settings.....	71

List of Figures

Figure 1-1	The Electromagnetic wave propagation	4
Figure 1-2	Electromagnetic frequency spectrum and associated wavelength....	5
Figure 1-3	Infrared rays wavelength dependent absorption.....	8
Figure 1-4	Microcapsule contains immiscible liquid phases.....	16
Figure 1-5	Functional nanometer magnetic particle.....	17
Figure 1-6	Endocytosis of albumin coated iron oxide nanoparticles (see arrow) attached to the cell membrane.....	18
Figure 1-7	The Hyperthermia applicator system.....	20
Figure 1-8	(a)The latest magnetic guidance system [ETD]. (b) Guidance of 0.014 inch wire using Stereotaxix system.....	20
Figure 1-9	FERX permanent magnetic guidance system by <i>FeRxTM</i> and application.....	21
Figure 1-10	Typical experiment setting of a calorimetric measurement.....	22
Figure 2-1	Magnetic responses with respect to different size of magnetic materials.....	26
Figure 2-2	The Ferro particle critical size vs. magnetic field frequency.....	27
Figure 2-3	Energy deposition rate. Material Fe_3O_4	29
Figure 2-4	Grain size dependent loss power density of Néel relaxation.....	31
Figure 2-5	Comprising of size dependent of hysteresis and Néel relaxation losses.....	32
Figure 2-6	Brownian relaxation with respect to grain size and viscosity.....	33

Figure 2-7	Time constant vs. particle size.....	34
Figure 2-8	Magnetic flux and infinity conductor.....	35
Figure 2-9	The skin depth of skin tissue and iron as a function of frequency....	38
Figure 2-10	Energy dissipation due to convection and radiation.	43
Figure 2-11	Stress & strain relation of plastic engineering material.....	44
Figure 2-12	Stress & strain relation of plastic engineering material.....	42
Figure 3-1	The relaxation iteration flow.....	46
Figure 3-2	Flow diagram showing implementation of a multi-field solver.....	49
Figure 3-3	Iron embedded fibre and cross section.....	51
Figure 3-4	Cross-sections of human torso placed in a magnetic field.	52
Figure 3-5	Micron size iron particle temperature dependent resistivity.....	55
Figure 3-6	Iron B-H curve in 1MHz field.....	56
Figure 4-1	Model geometry of 2-D simulation.....	57
Figure 4-2	The magnetic intensity of the cross-section with infinite element ...	59
Figure 4-3	The magnetic intensity of the cross-section without infinite element.....	59
Figure 4-4(1)	Induced heat power of embedded iron studs and human tissues at 1.0MHz, 2.6kA/m field.	60
Figure 4-4(2)	Comparing of energy density in various mechanisms.....	61
Figure 4-5	Temperature distribution of the tissues and fibre.....	61
Figure 4-6	The temperature distribution of fibre section after 0.002 second of heating.....	62
Figure 4-7	Temperature rise vs. time due to magnetically induced heating	

	in magnetic field of 2.6kA/m and 1.0MHz. Heating time is 0.002 seconds.....	63
Figure 4-8	Thermal bending of the fibre at $80^{\circ}C$, units in μm	63
Figure 4-9	Fire model used in 3-D FEM analysis.....	65
Figure 4-10	(a) A simplified cross-section of human torso. (b)The Fibre with embedded iron studs.....	65
Figure 4-11	A comparison of energy density of fibre components and tissues in two modeling, using the same initial resistivity of $0.3 \times 10^{-5} \Omega m$ of iron. Other parameters are the same as Figure 4-6.....	66
Figure 4-12	Temperature distributing in the 3-D simulation. Iron resistivity is fixed at $0.3 \times 10^{-5} \Omega m$	67
Figure 4-13	Temperature distributing in the 3-D simulation. Iron resistivity is fixed at $0.5 \times 10^{-5} \Omega m$	67
Figure 5-1	The fibre temperature as a function of iron resistivity Magnetic field flux intensity 2.6kA/m, frequency 1.0 MHz. Heating time is 0.002 seconds.....	69
Figure 5-2	The temperature of fibre, skin as the resistivity of the tissue changing with other parameters as the Figure 5-1.	70
Figure 5-3	The temperature of iron fibre and skin with respect to different frequency. The other parameters are the same as that of Figure 5-1.....	71
Figure 5-4	The tip displacement (μm) of the fibre as a function to temperature. The other parameters are the same as that of Figure 4-6.....	72

Chapter 1

Overview

1.1 Introduction

The purpose of this thesis is to consider externally activating a fibre inside the alveoli of a human lung. The primary concern is to examine the current available theories in field energy dissipation. It is hypothesized that the control of energy deposition inside the fibre in vivo is feasible given an oscillating magnetic field and ferromagnetic studs embedded inside the fibre. This work is inspired by the need for targeted, controlled release of drugs and general nanotechnology. The current nanotechnology initiatives are motivated by the added functionality derived from reducing the overall size of working systems. Targeted, controlled drug delivery deploys drug intact to specifically targeted parts of the body through a medium that can control the object's administration by means of either a physiological or a chemical trigger. A general overview of the current field energy dissipation theories is presented in the first section. Next, theories of magnetic field energy dissipation are explored. Following is a general description of Multiphysics coupled analysis. FEM model are introduced with parametric studies. Finally, the end discussion summarizes results and provides recommendations for future research.

1.2 Background

The word fibre depicts an object which has a high aspect ratio with axisymmetric or near axisymmetric cross-section. Due to its special geometry, fibres are usually pliant and can stand a bending deformation of large curvature. Natural fibres are

mainly composed of cellulose, while synthetic fibres have been made of nylon, polyester, acrylic and polyethylene, etc. Typical cotton fibre dimensions are 25 mm x 22 μm . The fibre being studied in this thesis is categorized as fibre fines, 0.1~0.5 μm in diameter and dozens of micrometers in length.

Actually, we eat lots of fibres everyday. The two types of fibre in food are soluble and insoluble. Soluble fibre, found in bean, fruit and oat products, dissolves in water and is thought to help the digestive process, lower blood fats and control blood glucose. Insoluble fibre, found in whole grain products and vegetables, passes directly through the digestive system, helping the body to get ride of waste products.

Synthetic fibre offers superior strength, dimensional integrity and weatherability in applications as diverse as plastic molded items, batteries and upholstery. Optical fibre can transmit nearly 80 gigabits of digital information per second; short synthetic fibres are woven into clothes. But their application in bio-engineering is still very limited. Fibres can bring adverse side effects to human body, e.g., they are carcinogenic when inhaled. Though of these concerns, externally activation of a fibre may introduce new applications otherwise hard to achieve.

From the point of view of mechanical engineering, to activate a fibre means to enforce the deformation of the fibre, i.e., extension, bending and cracking. If the fibre is isotropic in thermal expansion, the heating will result in a uniform volume expansion. However, if the fibre is composed of several materials with different thermal expansion ratio, the fibre will bend or even twist during heating. In this paper, we will study a way of externally induced fibre thermal bending.

The target is to externally induce heating inside a piece of fibre for the purpose of thermal bending. The fibre is 20 micrometers in length and airborne inside the

alveolar duct of a human lung. Direct heating of the fibre is difficult to manipulate, as the cross-section of the fibre is sub micrometer and it is inside the human body. Externally inducing heating of a fibre obviously involves the transmitting of energy through field propagation. This method implies several constraints on the energy source. First, the energy source must apply differential heating of the fibre and surrounding human tissues; second, field energy propagation must bring no biological side effects to the human tissue except insignificant thermal heating.

1.3 Sources of Field Energy

There are several mature technologies for transmitting energy through field propagation. Among them, ultrasonic, microwave and laser technologies are already available in clinical applications.

Ultrasound stands for the sound waves having frequencies higher than those to which the human ears can respond (about 16kc/s). They are usually divided into two categories according to their usage, low-amplitude propagation and high-energy [1]. Low-amplitude propagation can be used for the non-destructive testing of materials (e.g. ultrasonic imaging). The characteristic impedances and absorption coefficients of different material or the same material in different status render these applications highly successful. High-energy ultrasonic waves will cause a nonlinear relationship between the applied stress and resultant strain to the media it passes through. Ultrasound can be explored to derive therapeutic results by using its bio-effects such as creation of mechanical vibrations, localized cavitations, micro stream formation, physicochemical changes and thermal energy. As an application, high energy ultrasonic is used to disrupt cells by cavitation, damage body tissues by agitation, and

heat bone and muscles. Extensive *in vitro* and animal investigations during the last several decades have laid a foundation for ultrasound energy to be used for treatment purposes in various medical specialties. An important advantage of high-energy ultrasonic waves is that they are easy to focus. Obviously, the high-energy waves have the potential to be the source of the field energy for fibre thermal bending

Electromagnetic waves are normally composed of electric and magnetic vector (Figure 1-1). The TM mode depicts a mode for which the magnetic vector is zero; the TE mode depicts the mode whose electric vector is zero. The applicable electromagnetic wave composes a frequency range of 300KHz to 100GHz [2]. This range will then be divided into three sections. RF is typically used to refer to frequencies ranging from 300KHz to 300MHz; microwave is usually used for the range of 300MHz to 1GHz. And over 1GHz, we usually call them infrared or laser waves (figure 1-2) [2]. Current utilization of electromagnetic waves includes: noninvasive sensing, radiometry and thermograph, diagnostic imaging and hyperthermia treatment for cancer.

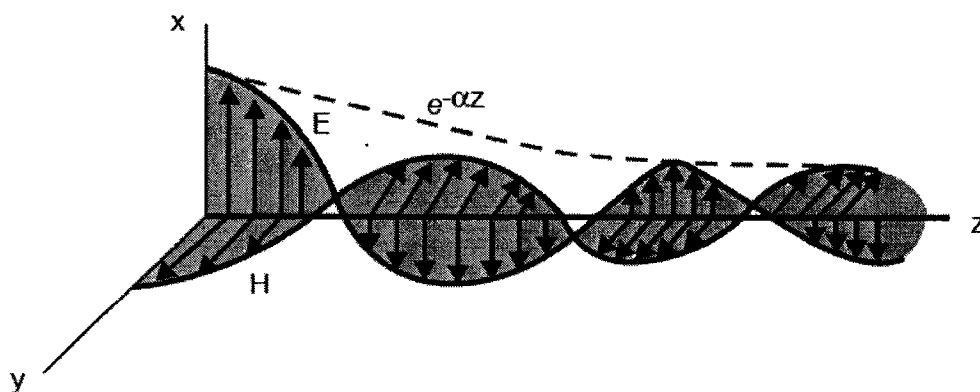


Figure 1-1 The electromagnetic wave propagation [3].

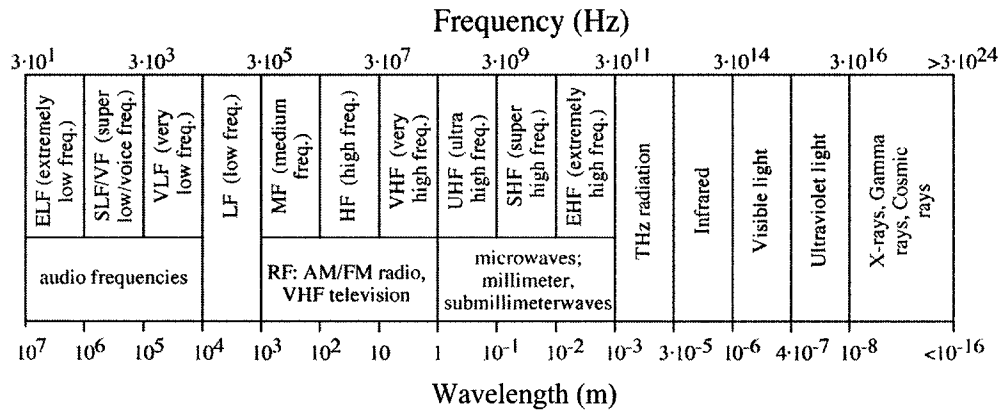


Figure1- 2. Electromagnetic frequency spectrum and associated wavelength [3]

1.4 Comparing of Field Energies

Table 1-1 list the general characteristics of ultrasonic and electromagnetic waves.

The ultrasonic wave is good at focusing and easy to manipulate. Exposure to ultrasound dissipates more energy to tissue than exposure of tissue to other types of radiation such as infrared radiation, diathermy or ultraviolet radiation. Absorption of energy transmitted by ultrasound depends on the attenuation coefficient α_1 , which is specific to the tissue. Tissue with high protein content usually absorbs more ultrasonic energy while tissue with high water content absorbs little. However, most ultrasound field energy is reflected when encountering an air/solid interface. The reflection rate is calculated as:

$$R = \left[\frac{Z_2 - Z_1}{Z_2 + Z_1} \right]^2 \quad (1-1)$$

The characteristic acoustic impedance Z of air is around 0.34, while it is over 1000 for human tissue. A reflection factor of $R=1$ means approximately no ultrasonic energy can penetrate an air/solid interface. Obviously, ultrasonic waves are not suitable for heating a fibre inside the alveolar duct of the human lung.

Table 1-1 List of field energy resources and governing Equations

	Ultrasound	Electric Wave	Infrared	Magnetic Wave
Sour.	Piezoelectric film	Waveguide, antenna	Laser beam	Coil
Freq.	1-100MHz 1.5mm-150μm	300KHz-100GHz 1m~1mm	30-0.3μm	200KHz- 200MHz
Refle.	$R = [(Z_2 - Z_1)/(Z_2 + Z_1)]^2$ $Z = \rho c$ ρ : density of the medium c : the speed of sound in that medium R : reflection coefficient	$R = [(\sqrt{\epsilon_1} - \sqrt{\epsilon_2})/(\sqrt{\epsilon_1} + \sqrt{\epsilon_2})]^2$ $\epsilon = \epsilon_0(\epsilon_r - j\sigma/\omega\epsilon_0)$ $\omega = 2\pi f$ ϵ_r : Dielectric constant ϵ_0 : Free-space permittivity σ : Conductivity ω : Radian frequency	$R = [(N_2 - N_1)/(N_2 + N_1)]^2$ $N_i = v/c$ v : electromagnetic waves speed in the medium(m/s) c : Light velocity in a vacuum (3e8 m/s) R : reflection coefficient	
Atten.	$I_x = I_o e^{-2\alpha x}$ $\alpha = \alpha_1 f^m$ α : Proportional to the square of the acoustic pressure α_1 : Attenuation coefficient at 1MHz (0.07-3) f : Frequency in MHz m : Lie between 0.76 (tendon) and 1.14(brain) Attenuation can be expressed also in terms of intensity:	$E = \frac{E_0^2}{2 \eta } e^{-2(\alpha z - j\beta z)}$ $\alpha = \omega \sqrt{\frac{\mu\epsilon}{2} \left[\sqrt{1 + \left(\frac{\sigma}{\omega\epsilon}\right)^2} - 1 \right]}$ $\beta = \omega \sqrt{\frac{\mu\epsilon}{2} \left[\sqrt{1 + \left(\frac{\sigma}{\omega\epsilon}\right)^2} + 1 \right]}$ $ \eta = \frac{\sqrt{\mu}}{\sqrt[4]{1 + \left(\frac{\sigma}{\omega\epsilon}\right)^2}}$ E_0 : Maxim value of the incident energy μ : Permeability	$I_x = I_o e^{-2\alpha x}$ In the nearby infrared regions of 600nm to 1.5μm, the tissue presents a transmission window for the electromagnetic radiation. Diffusion predominates over absorption in this band, to which the diode, colorant, Nd:YAG, Alessandrite and He-Ne laser emissions all belong, and consequently the penetration depth, in the order of 1-5 mm, is determined by multiple diffusion phenomena rather than by absorption	$E = H^2 f^{0.5} \mu^{0.5} a$ or $\frac{\mu_0^2 \omega^2 H_0^2}{\rho} \left[1 - \exp\left(-\frac{2\xi}{\delta}\right) \right]$ E : Absorbed power density (Wm ⁻³) per unit length seed H : Amplitude of magnetic field f : Frequency of magnetic field μ : Permeability a : Radius of the seed

Laser systems within the wavelengths range of 800-1100 nm are used to denature pathillogical tissue by local thermal effects. Other application includes cutting tissue by vaporization.

Lay[4], reported a model to efficiently absorb impinged laser energy in a slab by doping it with impurities for which the electrons have a resonance at the laser wavelength. His model showed, as an example, a laser wavelength of 248nm, a resonance width of 0.005nm, and impurity concentration of $\delta = 10^{-4}$ ($N = 1.43 \times 10^{17} \text{ cm}^{-3}$), the energy absorption efficiency becomes a maximum of $A \approx 85\%$. In his model, even with the laser frequency at a rather large deviation of 1% from the resonant line, 10% of laser energy may still be absorbed.

The absorption properties for human tissue in the near infrared are mainly determined by the absorption of water and endogenous constituents such as hemoglobin, melanin, bilirubin, etc. The scattering is caused by inhomogeneity of the refractive index of cellular structures. The scattering coefficient decreases from visible to infrared light. The optical properties of material can be defined by absorption coefficient $\mu_a [\text{mm}^{-1}]$, the scattering coefficient $\mu_s [\text{mm}^{-1}]$ and the phase function with anisotropy factor g [$-1 < g < 1$] [5]. For human tissues, g is known to range from 0.80 to 0.95. The scattering coefficient μ'_s can then be defined as[5]:

$$\mu'_s = \mu_s (1 - g) \quad (1-2)$$

The infrared rays will penetrate the human tissues at a wavelength near 600nm with a minimum water absorption rate (Figure 1-3) [6]. While the water absorption rate increases from the visible spectrum to the infrared region, for most other tissues it decreases in this range. This leads to an optical window, where the energy absorption

of biological tissue is relatively low. The effective penetration depth d_{eff} of laser light in the near infrared can be approximated by an analytical expression:

$$d_{eff} = 1 / \left(\text{sqrt} \left(3\mu_a (\mu_a + \mu_s') \right) \right) \quad (1-3)$$

This equation gives a penetration depth of less than 12mm of human tissues. So, the fibre inside the lung will hardly be heated by the commonly used laser sources since the penetration required is at least 100mm .

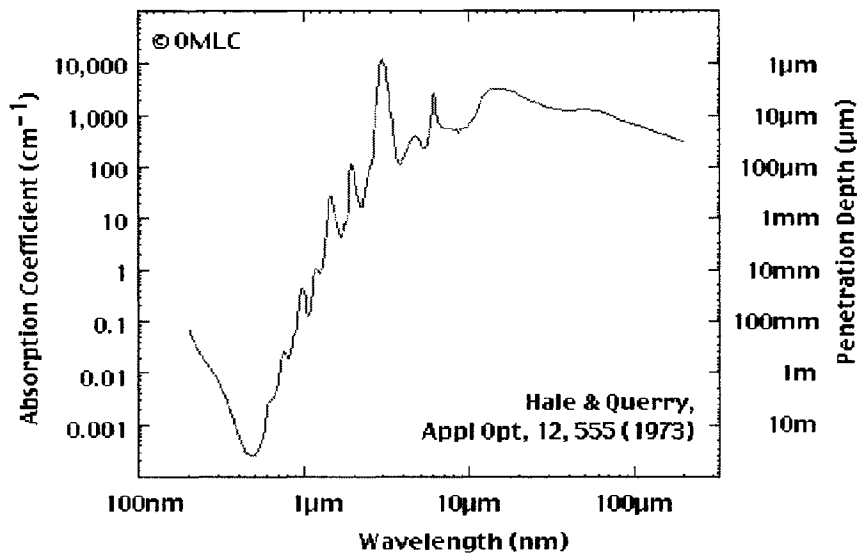


Figure 1-3 Infrared rays wavelength dependent absorption

The dielectric properties of human tissue make it unsuitable for the TM model of EM waves. The dielectric permittivity of biological materials in the RF and microwave range is largely determined by cell membranes and tissue's water content. The permittivity of human tissue is in the range of 100 to several thousand in the RF range [7]. "Electric fields are greatly diminished by many orders of magnitude inside biological tissues from their values in air external to the tissues. For example, an external field of 1kV/m may induce an electric field within the body of

about $1\text{mV}/\text{m}$. It is observed that electric fields induced inside the bodies of humans and animals are generally less than 10^{-7} of the field outside the body and rarely exceed about 10^{-4} of the external field “ [8]. This strength is near the typical strength at ground level beneath a high-voltage power line. This low-level voltage will generate currents, which are orders of magnitude weaker than the currents induced naturally from the function of heart, nerves, and muscles [9]. Electrical properties of tissues are frequency dependent in that, dielectric constant decrease and conductivities increase with increasing frequency.

Biological tissues behave like solutions of electrolytes that contain polar molecules at radio frequency electromagnetic field. The electrical component of EM waves will interact with biological system by ways of ionic conduction (oscillation of free charges) and rotation of polar molecules of water and protein relaxation. The absorption of RF energy is transformed into kinetic energy of molecules, which is associated with a rise in temperature of the irradiated tissues. Thus if being impinged on by a microwave, the human tissue will absorb much of the electrical field energy.

Human tissues are of comparably high electrical resistivity, but their magnetic permeabilities are equal to that of free space. This means magnetic waves can pass through human tissue in a far less attenuated way. Thus the electromagnetic TE wave is by far the best candidate as the energy field source for this specific application. In a historic perspective, the nineteenth century saw rapid development in medical applications and physiological effects of magnetism. But speculations regarding bio-effects due to exposure to electromagnetic field also began. In the next section, we will review the biomedical safety issue regarding electromagnetic human tissue interactions.

1.5 Bio-effects of Electromagnetic Tissue Interactions

Many researches are actively working to explain the interaction of EM fields with biological systems. The basics of EM interaction with materials were elucidated over a century ago and stated as the well-known Maxwell and Faraday's equations. Application of these theories to biological systems, however, is very difficult because of the extreme complexity and multiple levels of organization in living organisms, in addition to the wide range of electrical properties of biological tissue. Tissue interaction with EM fields have been extensively studied in terms of several quite different endpoints; in their thermal effects, in the magnetic force in microscopic level and in ionization of atoms in bimolecular systems [10].

In an oscillating magnetic field with a frequency up to MHz, a biological material is regarded as a conducting medium. As in the microscopic level, all tissues are composed of cells and extra cellular fluids. A cell has two parts: the outer insulating membrane and the inner cytoplasm and nucleus. The extra cellular fluid has high conductivity. Cells appear to be insulators and almost all the currents induced in tissues by EM fields will flow around the cells. The insulating membrane, which completely surrounds the conducting core, makes the cell itself a series combination of the membrane capacitance and the cytoplasm resistance.

Oscillating magnetic fields will generate eddy currents at cell membranes and in tissue fluids, which will circulate in a closed loop that lies in a plane normal to the direction of the magnetic field. The current density in a circular path perpendicular to a sinusoidal magnetic field is derived from Faraday's law of induction [11]

$$J = \pi \sigma r B f \quad (1-4)$$

where J is the current density in *Amperes/meter*² (A/m), σ is the conductivity of the medium in *siemens/meter* (S/m), r is the radius of the loop for inductive of current in *meters* (m), B is the magnetic flux density in *teslas* (T) or *Webers/meter*² (Wb/m^2), and f is the frequency in *Hz*.

Due to the comparably low electrical resistivities of human tissues, a very high frequency (up to 100 MHz) will induce eddy currents that may cause damage to biological systems. At a frequency below approximately 100 kHz, currents necessary to heat biological systems are usually less than currents necessary to stimulate neurons and other electrically excitable cells [8].

Thermal effects can be defined as energy deposition rate higher than the thermoregulatory capacity of the human body. The heat generated by the basal metabolism for a 70-kg man is approximately $1.2 W/kg$. For adverse health effects, such as eye cataracts and skin burns, to occur from exposure to RF fields at high frequencies, power densities above $1000 W/m^2$ are needed.

There are speculations over biological effects that occur under circumstance of no evident change in temperature or the exposure level is low enough not to trigger thermoregulation in the biological body. Literature shows an exposure to low level EM waves (less than $2 W/kg$) could affect the nervous system [12]. Also, a magnetic oscillation field might affect the immune system, gene and chromosomal morphology, enzyme activity, neurological function, cell morphology, etc. But, literature on these effects are usually contradictory and the mechanisms of the effects are not well understood.

Biological magnetisms, the essentially components of living system, are usually found in single domain units, wrapped with thin magnetosomes. These microstructures behave like small magnets and are influenced by external fields to change their energy contents. It is believed also that they will orient with the applied magnetic fields. Magnetosomes exist in the interior of cells bound to cell bodies through cytoskeleton. In such gathering, torque generated by the action of the magnetic field acts to rotate the whole cell through forces on the individual magnetosomes that are magnetically lined up. Magnetosomes may reorient in the cell, which may create biological effects because they are not rigidly bound to the whole cell structure [8].

Free radicals are atoms or molecules with at least one unpaired electron. These unpaired electrons will change the structure of other molecules and cause them to also become free radicals if collide. Free radicals are remarkably short lived, existing for less than $1ns$. Their effect is extreme in terms of cell aging and various kinds of cancer because of the damage they do to DNA, cells and tissues. Static magnetic fields may influence the response rate of chemical reactions involving free-radical pairs. Since the lifetime of these free radicals is short compared to the cycle time of the RF field in general, the applied fields act like static fields during the time scale over which these reactions occur. Biological effects due to fields less than $50\mu T$ are not significant because any effect of field would be additive with a $30 - 70\mu T$ geomagnetic field [8].

Brocklehurst [13] studied the reactions of radical pair under the effects of external magnetic field. He anticipated that such effects are theoretically conceivable down to fields of strength as low as $0.1mT$. However, the effect observed was very small at

0.1 *mT* (1% increase in free radical concentrations). The fact is that the body possesses sophisticated defense mechanism to cope with these radicals under normal conditions.

Ionizing radiation poses hazards to living organisms through its destructive effects on key macromolecular system, where damage to DNA in the cell nucleus, for example, may cause permanent genetic changes transmitted as mutations to succeeding generations of cells. But as we are utilizing the electromagnetic wave with only the magnetic component, the ionizing radiation is ignored. The nonionizing radiation of magnetic field is not known to damage DNA in the way ionizing radiation does. The investigations of exposure to magnetic fields are also contradictory and usually the data are not replicable. Two reviews [14, 15] concluded that Radio frequency magnetic field is not directly genotoxic, but there may be other indirect effects on the replication and /or transcription of genes under relatively restricted exposure conditions.

Litovitz [16] hypothesized that AC electromagnetic waves need to be steady for certain period of time (up to the order of second) for a biological to respond. This allows cells to discriminate external fields from thermal noise fields, even though they might be smaller than the noise shields.

Melatonin is a hormone produced by pineal gland. It helps destroy the free radicals and cell division to take place with undamaged DNA. Melatonin also assists in regulating the female menstrual cycle and circadian rhythms. There are results from five cellular studies showing the EM fields will reduce the growth inhibitory action of melatonin on human breast cancer cells in culture [8]. In 2000, Graham

[17], found no effects on melatonin levels among young men volunteers exposed to 4 continuous night of 60- *Hz* fields at $28.3 \mu T$.

It is concluded from the three main biophysical mechanisms (induced electric currents, direct effect on magnetic biological materials, and effects on free radicals) that high field strength is needed to produce noticeable biological effects in living systems. However, we need also an understanding of how EM fields affect life process to understand the bio-electrochemical mechanism.

“Other studies on calcium transport, cell proliferation & differentiation, enzyme activity, hormones, immune system, etc. have also been reported. Overall, the literature shows that while some bio-effects of exposure to low frequency electric and magnetic fields take place. They are usually field amplitude dependent. It is unknown what the long-term effects of EM are and whether they are cumulative. It is important to note that modulated or pulsed EM waves seem to be more effective in producing an effect” [8].

From a large number of studies, it is concluded that electric and magnetic field exposures delivered at field strength similar to those measured for typical exposure below $0.1 mT$ do not produce any significant cellular effects such as genotoxic and epigenetic activity. It is generally accepted that the applicable range of frequencies and amplitudes in human cells is considered to be $f = 0.05 \sim 1.2 MHz$ and $H = 0 - 15 KAm^{-1}$ [18]. Atkinson concluded a field with $H \cdot f$ product lower than $4.85 \times 10^8 Am^{-1}$ is safe and tolerable [19]. Recently, Hergt [20], proposed a limit of $H \cdot f < 3 \times 10^9 A/(ms)$ (suitable for breast tumor treatment). That is, a field amplitude of $10 kA/m$ would allow a maximal frequency of $300 kHz$.

1.6 Experiments and Clinical Applications of Magnetic Field and Ferromagnetic Materials

The application of magnetic field and magnetic particles *in vitro* has been practiced for decades. Magnetic particles with size ranging from a few nanometers up to micrometers offer attractive opportunities in applications in magnetic resonance imaging (MRI), controlled drug delivery, hypothermic treatment of tumor cells, etc.

MRI technologies utilize the different signal each tissue produced in response to the applied pulses of radio frequencies. The MRI image of anatomical structure depends on collecting the induced magnetic moment of proton, which is different from tissue to tissue. Due to the small effect of magnetic field on collection protons, roughly equal to only three of every million proton moments m , a contrast agent will sharpen the contrast by affecting the behavior of protons in their proximity. The most common contrast agents currently used are colloidal iron oxides in size varying from 10 to 500nm.

Text resume at page 17.

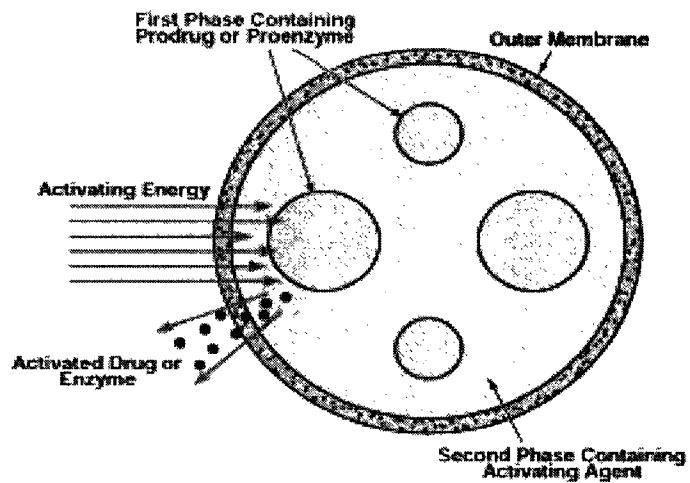


Figure 1-4 Microcapsule contains immiscible liquid phases. The first phase consists of spheroids containing a prodrug or a proenzyme. The second phase is the surrounding liquid containing an activating agent. Exposure to electromagnetic or energy would cause activation, after which the drug would diffuse through outer membrane to act on surrounding tissues.[21]

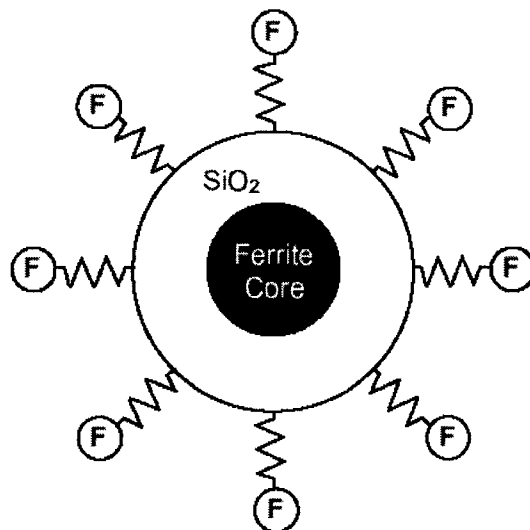


Figure 1-5 Functional nanometer magnetic particle [18]

Targeted drug delivery aims to promote active compound accumulation in the body target zone independent from the method and route of drug administration (i.e. Figure 1-4). Amongst the current principles of drug targeting is magnetic targeting, i.e. the drug or radionuclide can be immobilized in biocompatible magnetic nano or microspheres or in magnetoliposomes. Generally, the magnetic component of particles is coated by a polymer of dextran or PVA. The carrier usually is made of one of the following forms: (i) a particle core of magnetic (Fe_2O_3 or Fe_3O_4) coated with biocompatible polymer (Figure 1-5) ; (ii) magnetic nanoparticles precipitated porous polymer [18]. The carrier is often associated with another molecule capable of specific recognition and binding to the target site, i.e. binding for a given organ or on individual component characteristics such as cell surface. Lübke [22], explored the first clinical magnetic drug targeting by using a Ferro fluid (100 nm) to which the drug was chemically bound. Current technologies can achieve the localization of up to 70% of the functional dose in the target tissue, with minimal interaction and toxicity to normal cells. An up to eight-fold increase in drug concentration after administration of only one third of the drug dose has been observed [23].

Text resume at page 18

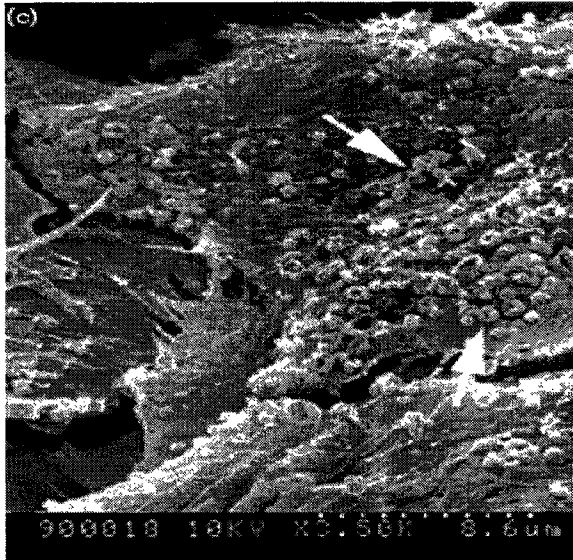


Figure 1-6 Endocytosis of albumin coated iron oxide nanoparticles (see arrow) attached to the cell membrane [22]

Hyperthermia is a promising approach to cancer therapy based on the fact that the tumor cells are ten times more sensitive to temperature rise than normal cells. Hyperthermia therapy heats the target tissue to temperatures between 42 to 46^oC thus reducing the viability of cancer cells, increasing their sensitivities to chemotherapy and radiation or enhancing the capability of anti-tumor drugs [23]. In the past, external means of energy dissipation such as ultrasonic or microwave treatments were used, but more and more experiments are employing magnetic particles as a media to heat the target cells. Magnetic hyperthermia is based on the theory that magnetic particles will produce heat through various kinds of energy losses when placed in an external AC magnetic field (Figure 1-6). The heating capability of these particles is proportional to the strength of external magnetic field, the particle size and the AC frequency. In most cases, the controlled heating can also be achieved by controlling the material Marie Curie temperature, that is, the

temperature above which the material lose its magnetic property and thus its ability to heat.

Gilchrist [24], succeeded in heating 20-100nm $\gamma\text{-Fe}_2\text{O}_3$ particles by exposing them to a 1.2 MHz magnetic field. Gordon [25], was the first to use a magnetic fluid based on dextran magnetite nanoparticles to treat malignant tumor on rats. Other authors have studied suspensions of magnetic particles for treatment of malignant cells [26, 27]. Hamad-schifferli [28],linked DNA and protein with a 1.4 nm gold particle. By exciting eddy currents in the latter through a 1GHz magnetic field, he succeeded in dehybridizing the DNA in a manner that is localized and reversible.

There are also fundamental problems associated with the use of magnetic particles in the above applications. There is a size dependent collection mechanism: nanoparticles with diameters of 30 nm or more are rapidly collected by the liver and spleen, while particles with sizes of 10 nm or less are not so easily collected. These small particles, finally collected by the reticuloendothelial system, will have a longer half-life time in the blood [18]. Targeting to some specific cell types, in retaining the particles localized at the cell membrane, is difficult as the cell tends to instigate receptor-mediate endocytosis [22]. The applied magnetic field strengths may not be strong enough to build up and sustain field strength sufficient to counteract the linear blood flow rates in tissues so as to effectively retain the drug carrier at a specific place. There are also potential downfalls of the toxicity of the iron, which directly relates to the body's ability to rid itself of excess iron.

Hyperthermia requires an AC magnetic field applicator system. This system must match the limitation of field strength and field-frequency as the highly conductive tissue will also be heated during the therapy [29]. The first prototype of clinical

hyperthermia clinical system was set up in Charité Medical School, Campus Virchow-Klinikum, Clinic of Radiation Oncology in Berlin. Figure 1-7 shows their latest model. This ferrite-core system operates at a frequency of 100kHz with adjustable field strength from 0 to 15kA/m.

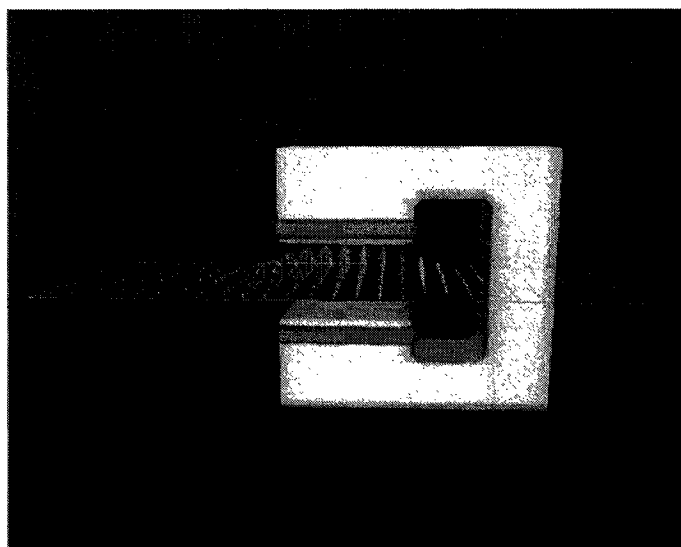
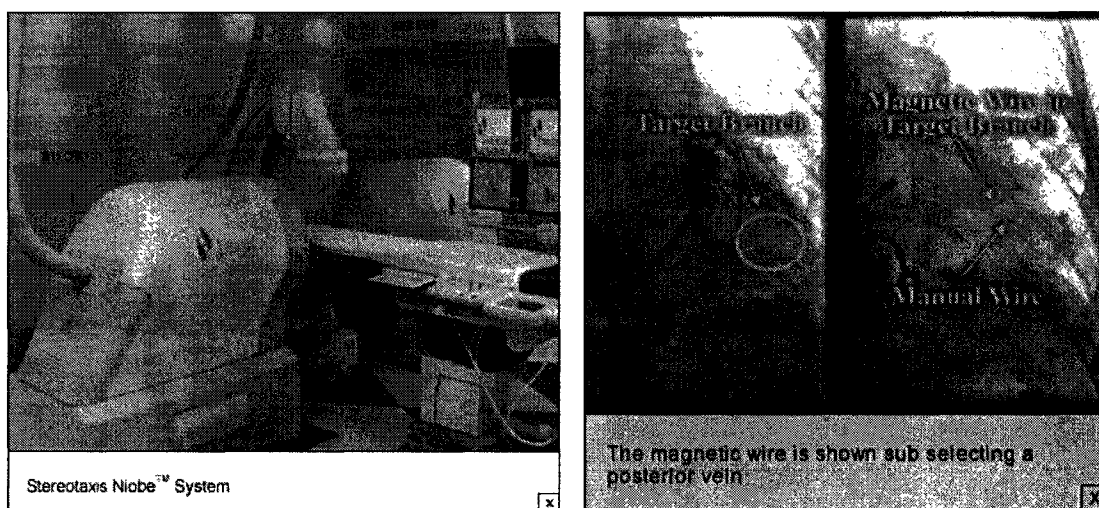


Figure 1-7 The Hyperthermia applicator system [30]



(a)

(b)

Figure 1-8 (a) The latest magnetic guidance system. (b) Guidance of 0.014inch wire using Stereotaxis system [31].

There are two FDA approved magnetic systems available on the market. The latest prototype magnetic guidance system is a 6-coil superconducting multicoil helmet built by Wang NMR as a fifth generation device (Figure 1-8). The next generation of magnetic Stereotaxix system is more compact and more cost effective.

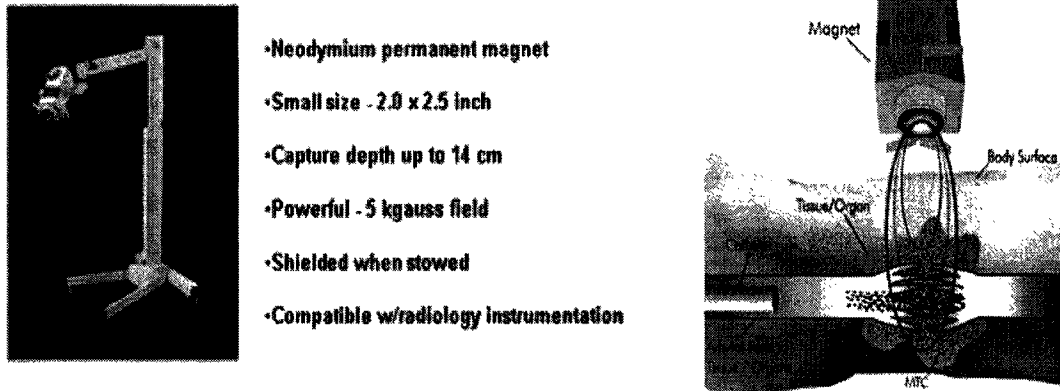


Figure 1-9. FERX permanent magnetic guidance system by *FeRxTM* and application [32].

Another FDA approved system is *FeRxTM* (Figure 1-9). The mechanism and apparatus of this machine are shown in Figure 1-9. The FERX system is applied on the target organ and interrupted every 15 minutes to ensure blockage of the main arteries has not occurred.

The experimental measurement of heating capacity of ferromagnetic materials in an oscillating magnetic field usually adopts the configuration shown in Figure 1-10 [33].

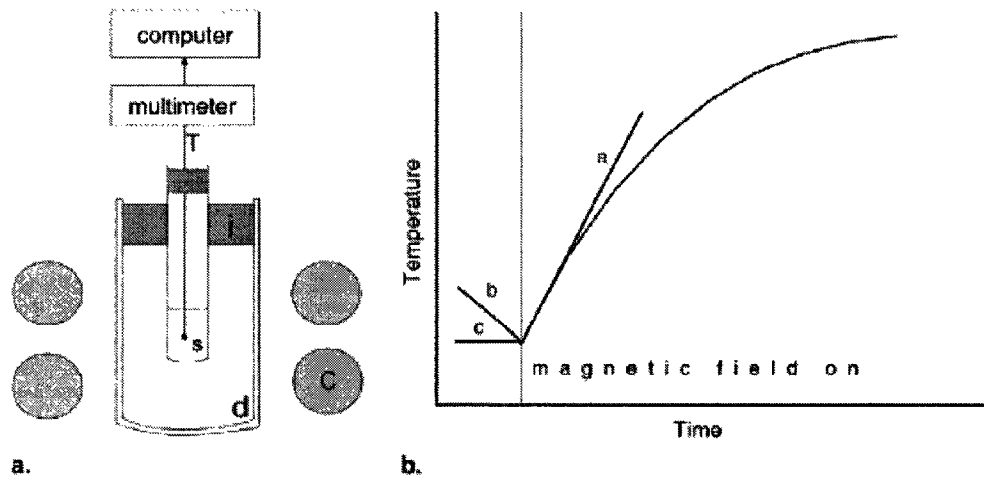


Figure 1-10 Typical experiment setting of a calorimetric measurement. (a) experimental setup. (b) Schematic temperature curve [33].

In Figure 1-10. T, I, d, and c stands for thermosensor, isolation, suspended ferro oxide particles, vacuum vessel, and the coil, respectively. The special absorption rate (SAR) of the ferrofluid in the alternating magnetic field was measured calorimetrically by registration of the temperature increase in the ferrofluid after applying the AC-field.

Chapter 2

The Electromagnetic Field Energy Deposition

2.1 Basic Concept of Magnetic Materials and Magnetic Field

If a piece of magnetic material is placed in a magnetic field of strength H , the individual atomic moment in the material contributes to its overall response. The magnetic induction B is given by:

$$B = \mu H = \mu_0 H + \mu_0 x H \quad (2-1)$$

where μ_0 is the permeability of free space, x is the dimensionless susceptibility. When x falls in the range of $10^{-6} \sim 10^{-1}$, these materials are called paramagnets; when x falls in the range of $-10^{-6} \sim 10^{-1}$, these materials are called diamagnets. Ferromagnetic materials exhibit a large susceptibility of $10 \sim 10^4$. Ferromagnetism is one of magnetic state of the substances characterized by parallel orientation of the magnetic moments of nuclear carriers of magnetism. It is caused by positive values of energy of inter-electronic exchange interaction. The magnetization, $M = \mu_0 x H$, grows not linearly with increase of magnetic field H and achieves a limit value M_s (magnetic saturation). Values of M_s depend also on "magnetic history" of the sample. It makes the dependence of M_s on H ambiguous, so that a magnetic hysteresis curve is observed.

Ferromagnetic hysteresis is characterized by several parameters: coercivity, remanence (or remnant magnetization), magnetization of saturation, maximum

energy product (or strength of the magnet). Coercivity H_c is the field which has to be applied to ferromagnetic material to make magnetization equal to zero. Remanence, M_r , is residual magnetization of a ferromagnetic material in the absence of external magnetic fields (after the external magnetizing field has been turned off). This parameter is convenient to use for comparison of the relative strength of different magnets. It depends greatly on magnet composition and method of manufacture. Magnetization of saturation is magnetization of ferromagnetic material in very strong (infinite strong) magnetic fields. All the atoms in this case are magnetized in one direction. Strength of the magnet is the area of hysteresis loop. This gives a measure of the energy stored in the magnet. The usual unit is the Mega Gauss-Oersted (MGOe). The SI unit is kJ/m^3 . [1 MGOe = 8 kJ/m^3].

Table 2-1: the list of magnetic field flux density [34].

Application	B field (Teslas)
Sensitivity of a scanning SQUID microscope	10^{-16}
Human Brain	10^{-13}
Intergalactic and interstellar magnetic fields	10^{-11}
Human heart	10^{-9} - 10^{-8}
Earth's magnetic field	0.5×10^{-5}
Refrigerator magnets	10^{-4} - 8×10^{-3}
Electron beam of CRT	5×10^{-4} - 10^{-3}
Magnetic read switch	10^{-3} - 2×10^{-3}
1-horsepower electric motor	0.1-0.2
Rare-earth permanent magnets	2
Magnetic Resonance Imaging	0.5-5
High-energy particle accelerators	10
World Record Continuous Field	45 T
Long-Pulse Magnet (800 ms)	60
Strongest Destructive Pulsed Magnet at NHMFL-Los Alamos (4-8 μs)	850
Neutron Stars	10^8

The susceptibility in ferromagnetic material depends not just on temperature, but also on magnetic field intensity and material atomic structure. For ferromagnetic materials, it displays no net magnetic poles without external influence, as the atomic magnetic moments align themselves in their least-energy state and cancel each other internally. Atomic magnetic moments are partially the result of electron orbits, so as temperature rises the orbital path lengthens and the strength of the magnetic moment decreases [35]. At high frequency, the permeability of bulk magnetic material, which is given by Snoek's law, also decreases [36]:

$$\mu = 1 + \gamma 4\pi M_s / f \quad (2-2)$$

where γ is the geomagnetic ratio (0.8661×10^7 at 3.231 MHz for iron), f is the operation frequency. The eddy current, in the high frequency, will cause a reduction in permeability. It is assumed that a decrease in electrical resistivity of material will enhance the eddy current loss and thus reduce permeability. Thin films of magnetic materials also show advantages in achieving high values of permeability [37, 38]. Iron-based ferromagnetic materials with high saturation and high permeability have been developed. They can achieve an electrical resistivity of 100~300 $\mu\Omega$.cm and a relative permeability of 3000 over MHz frequency [39, 40].

In amorphous solids the magnetocrystalline anisotropy is equal to zero, eliminating the main material dependent contribution to the coercivity H_c . At low frequency, the coercivity follows Sharrock's Law [41]:

$$H_c(f) = \left(\frac{2k}{M_s}\right) \left[1 - \left(\frac{kT}{kV}\right)^{1/2} \left(\frac{1}{2}\right) \ln f_0 \right] + \left(\frac{2k}{M_s}\right) \left[\left(\frac{kT}{kV}\right)^{1/2} \right] \left(\frac{1}{2}\right) \ln f \quad (2-3)$$

2.2 B-H Curves and Hysteresis Losses

The B-H curves of ferromagnetic particles are size dependent. Figure 2-1 shows the floated magnetic particles with respect to blood cell and their different B-H curves [18].

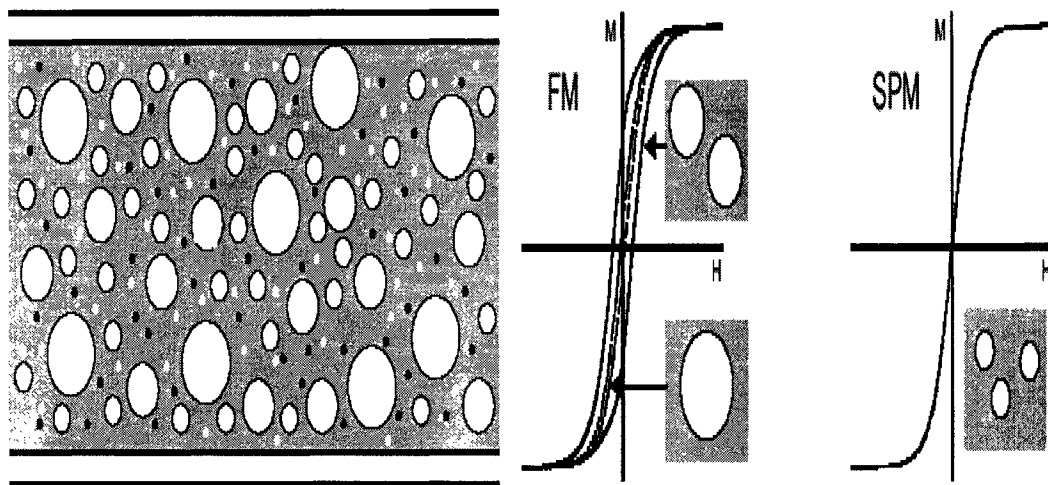


Figure2-1: Magnetic responses with respect to different size of magnetic materials, illustrated for a hypothetical situation in which particles of a range of size from nanometer up to micron scale are injected into a blood vessel. The response of ferromagnetic particles with response to magnetic field H can be either multi-domain (----- in FM diagram), single-domain (___ in FM diagram), or superparamagnetic (SPM), depending on the size of the particles [18].

The hysteresis loop showed in Figure 2-1 was first studied more than one century ago. The hysteresis behavior can be one or a combination of nucleation processes by the domain wall propagation or by retardation of the magnetization due to fluctuation [37]. In the framework of this study we study ferromagnetic material subjected to a field up to 4×10^{-3} Tesla at a frequency of MHz. Generally, the nucleation and domain wall phenomenon will be dominant. When the frequency and domain wall length are higher, the hysteresis area will be smaller in a domain wall

moving. The existence of defects in the magnetic materials brings the rise of nucleation hysteresis losses. This mechanism only works when the nucleation is the longest process or the average reversal time of nucleation is rather large in comparison to the oscillation period. The nucleation mediated hysteresis loop has a rectangular shape, whereas a curved shape indicates that the hysteresis is associated with the domain wall propagation or with strong oscillation of magnetization.

In large particles, of the size of micrometers and beyond, there exists a multi-domain wall state which leads to a narrow hysteresis loop since it takes relatively little field energy to move the domain walls; while in a smaller particle there exists a single domain wall which leads to a broad hysteresis loop, whereas nucleation of hysteresis will be dominant [18]. At even smaller size, of tens of nanometers or less, the magnetic moment of the particles is free to fluctuate with the thermal energy, while the individual atomic moment retains its order state. This leads to a hysteretic curve (SPM) shown in figure 3-1.

The hysteresis loss, which is nonlinearly dependent on the field amplitude, is usually referred to as a square law in the literature [42].

$$P_h = \pi\mu_0\chi_0H_0^2f \frac{2\pi f\tau}{1+(2\pi f\tau)^2} \quad (2-4)$$

where τ is the relaxation time, χ_0 is the actual field dependent susceptibility. Hysteresis loss is particle size dependent as the relaxation time τ is exponentially proportional to particle volume [43]:

$$\tau = \tau_0 \exp[kV/(kT)] \quad (2-5)$$

($\tau \sim 10^{-9}$ s), where V is the particle volume, K is the anisotropy energy density and kT is thermal energy. The remnant magnetization M_r and coercivity H_c will both decrease abruptly at some critical grain where $\omega \cdot \tau = 1$.

$$M_r = M_{r0} \exp(-t / \tau) \quad (2-6)$$

$$H_c = (2K / M_s)[1 - (V_c / V)^{1/2}], V > V_c. \quad (2-7)$$

Figure 2-2 shows in a magnetocrystalline anisotropy energy density level of $10^4 J/m^3$ and $10^6 J/m^3$, the critical particle size ranges from 30nm~5nm in up to 10^9 frequency.

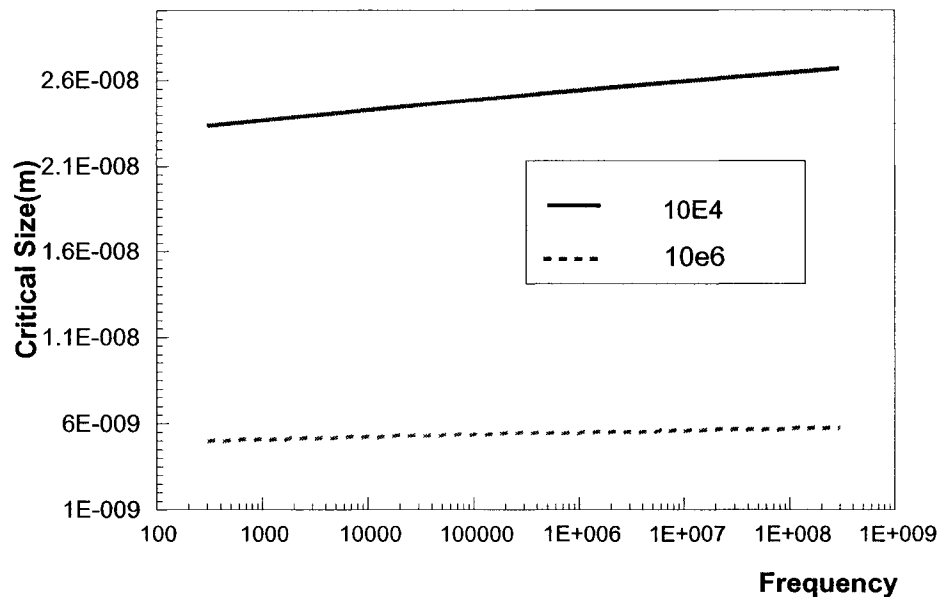


Figure 2-2. The Ferro particle critical size vs. magnetic field frequency.

Magnetocrystalline anisotropy energy density is of $10^4 J/m^3$ and $10^6 J/m^3$.

In particles with size greater than the critical value, the theoretically predicted energy dissipation value is very high (Figure 2-3), if neglects the fact that the unit heating capacity decreases due to the multi-domain wall state in the larger particles.

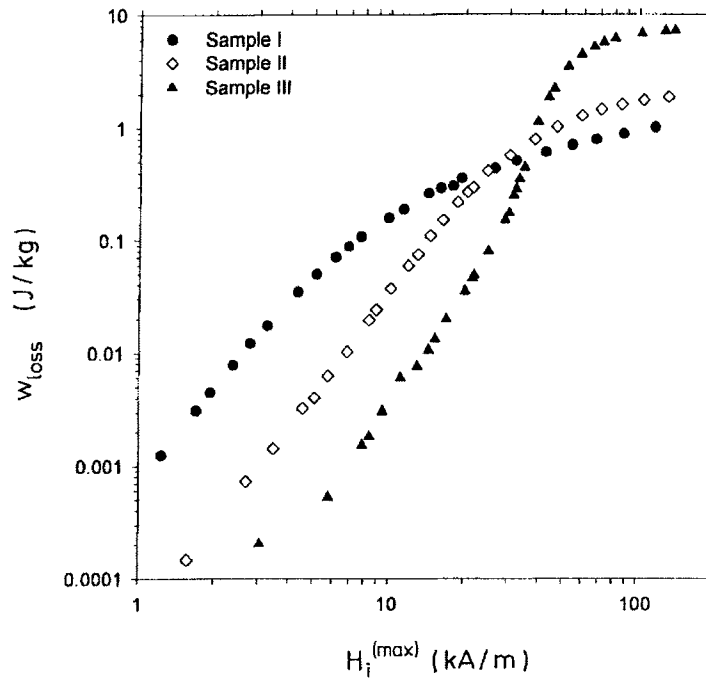


Figure 2-3 Energy deposition rate. Material Fe_3O_4 . sample I, >1000nm; sample II, 250nm; sample III, 60x250nm. Frequency 50Hz [43].

Experiments have been designed to investigate the heating capacity of ferromagnetic materials in an clinical approximation situation[20, 33, 43]. Table 3-1 shows a list of results from the literature. Obviously, experiment data show the accepted hysteresis energy loss is below 500W/g.

The sample III in Figure 2-3, with size of 60x250nm, is dominated by single domain behavior processes with large coercivity of 34kA/m and thus showing very high hysteresis losses [43]. However, because of the limitations on the amplitude of magnetic field to which human tissue exposing, only a portion of the hysteresis loop will be utilized in the hyperthermia.

Table 2-2. List of Ferro energy deposition experimental data

Author	Material size (nm)	Field intensity (kA/m)	Frequency (KHz)	Energy density (W/g)
Hergt et al. [43]	Fe_3O_4 , >1000	14	300	75
	Fe_3O_4 , 250	14	300	42
	Fe_3O_4 , 60x250	14	300	3
Hilger et al. [33]	Fe_3O_4 , >350	6.5	400	7
	Fe_3O_4 , 100	6.5	400	6
Hergt et al. [20]	Fe_2O_3 , 15	6~12	327~410	150~500
Toshifumi et al [44]	$Mg_{1+x}Fe_{2-2x}Ti_xO_4$	0.8~8	230	4~16
Cheng et al. [45]	Iron oxide, 1000	5	1	0.15×10^{-3}
Ma et al. [46]	Fe_3O_4 , 7.15~416	32.5	80	15.6~75.6

2.3 Néel Relaxation Losses

Ferromagnetic particles of the size approximately one nanometer are called “superparamagnetic” particles. These particles still possess considerable heating capabilities. The energy deposition is based on the theory that there are only two antiparallel orientations of the particle magnetic moment m . The corresponding two energy levels, namely n_+ & n_- are separated by an energy barrier given by the particle anisotropy energy kV [47]. In an external oscillation magnetic field, the transition probabilities are given as:

$$\omega_{\pm} = (1/2\tau) \exp[\pm mH / (kT)] \quad (2-8)$$

The exponential part may be replaced by a first order approximation for small fields when $mH \leq kT$. The magnetization is then given by [43]:

$$M(t) = (nm^2/kT)(1+i\omega\tau)^{-1} H_0 \exp(i\omega t) \quad (2-9)$$

$$(n = n_+ + n_-)$$

The specific power P for small field amplitude is [48]:

$$P = (mH\omega\tau)^2 / [2\tau kTV(1+\omega^2\tau^2)] \quad (2-10)$$

At low frequency, the losses increase with the square of frequency, a superparamagnetic regime; while for $\omega \cdot \tau = 1$, the losses saturate at

$$P = (mH^2) / (2\tau TV\tau)$$

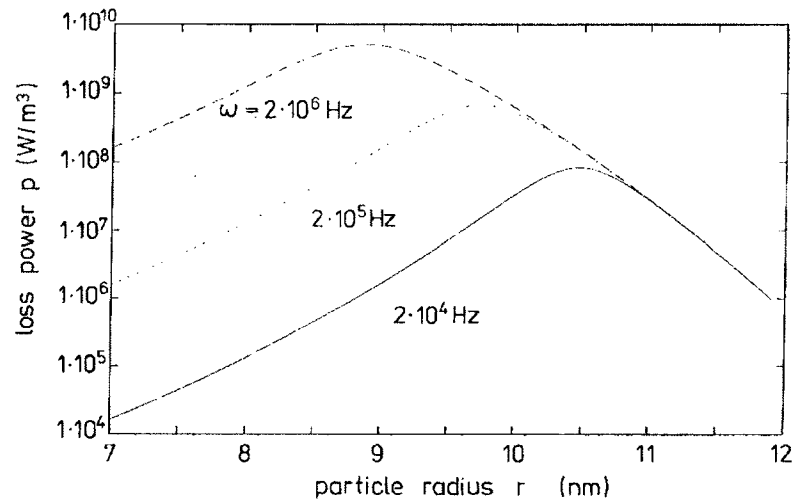


Figure 2-4 Grain size dependent loss power density of Néel relaxation. Field amplitude $6.5KA/m$, $M_s = 4.7 \times 10^5 A/m$ and $K = 10^4 J/m^3$ [43].

Both hysteresis loss and Néel relaxation loss are grain size dependent. Figure 2-5 shows the comparison between these two losses, assuming $M_{r0} = 0.5M_s$

$$H = 6.5KA/m, \omega = 2 \times 10^6 /s, M_s = 4.7 \times 10^5 A/m \text{ and } K = 10^4 J/m^3.$$

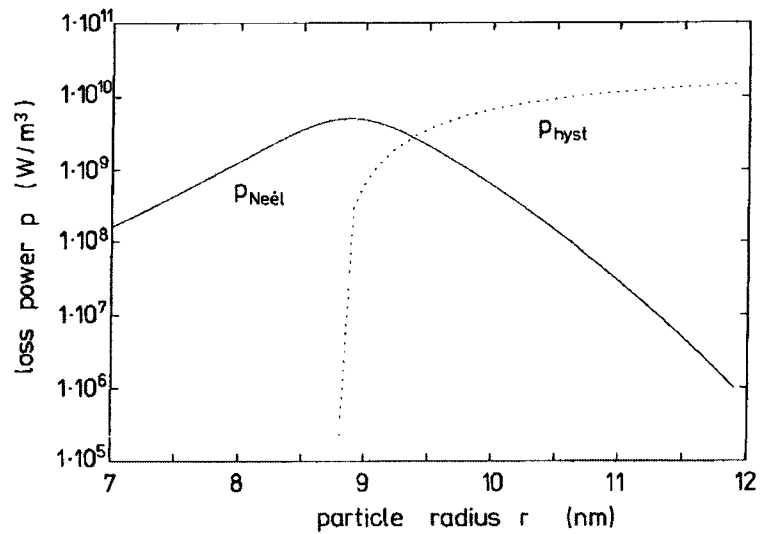


Figure 2-5. Comparison of size dependent of hysteresis and Néel relaxation losses [43].

From Figure 2-5, as the grain size decreases, the hysteresis losses increase until they decline abruptly at some critical grain size. The remanence M_r and H_c coercivity vanish depends on the oscillation frequency (Formula 2-6 & 2-7). In Figure 2-5, the critical grain size is around 9nm. Where the hysteresis losses nearly vanish, the Néel relaxation losses dominate and extend to even smaller particle size. By theoretical calculation the maximum Néel relaxation loss is only a fraction of hysteresis losses.

2.4 Brownian Relaxation Losses

Besides the above two heating mechanisms, the ferro fluids also involve relaxation loss due to rotational Brownian motion of magnetic particles. The Brownian relaxation losses will become essential if the magnetic moment direction is strongly coupled to the particle itself, e.g., by a large value of the intrinsic magnetic anisotropy, combined with easy particle reorientation due to a low viscosity η of the

suspension medium. For a spherical particles with the hydro dynamically radius r the relaxation time and power loss are given as [43]:

$$\tau_B = \frac{8\pi\eta r^3}{kT} \quad (2-11)$$

$$P = (mH\omega\tau)^2 / [2\tau kTV(1 + \omega^2\tau^2)] \quad (2-12)$$

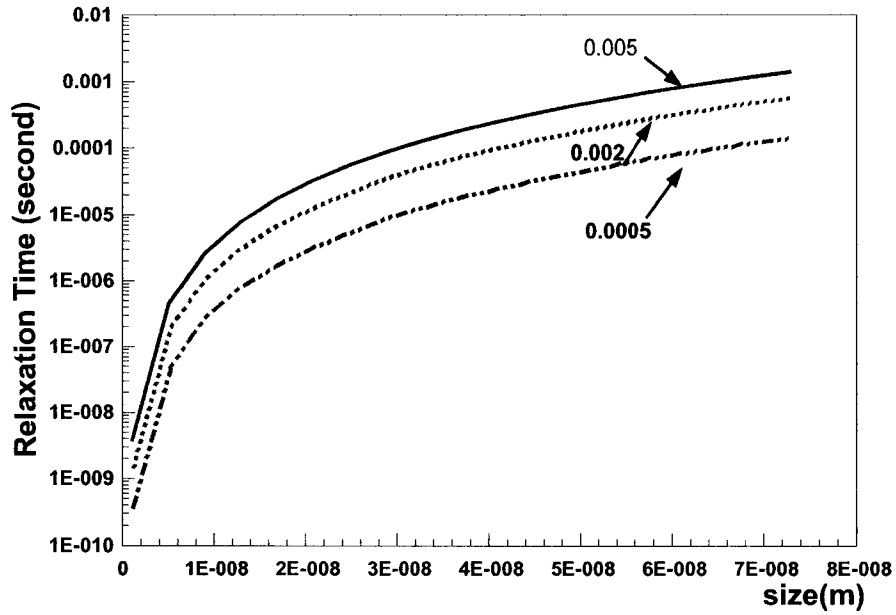


Figure 2-6 Brownian relaxation with respect to grain size and viscosity

Figure 2-6 shows the Brownian relaxation time τ is a weakly dependent on particle size. For a ferro fluid has a broad distribution of particle sizes with a mean size of ~ 10 nm, the Brownian and Néel relaxation process will both occur. The effective relaxation time τ is given by [42]:

$$\frac{1}{\tau} = \frac{1}{\tau_N} + \frac{1}{\tau_B} \quad (2-13)$$

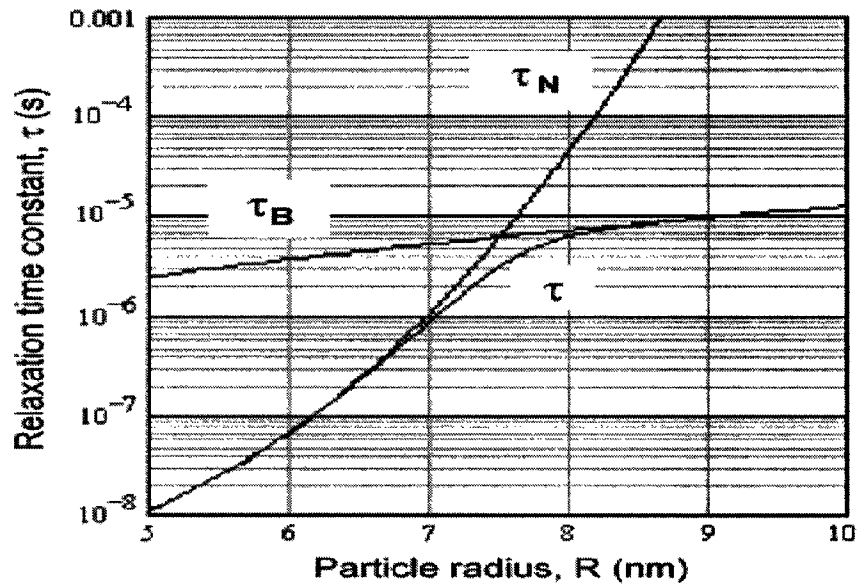


Figure 2-7. Time constant vs. particle size [42].

The Figure 2-7 illustrates that the shorter time constant tends to dominate in determining the effective relaxation time for any given size of particle.

2.5 Eddy Current Losses

The laws which describe the behavior of the electromagnetic force were first compiled into a self-consistent theory in 1864 by the Scottish physicist James Clerk Maxwell (1831-1879), and since then the theory of electromagnetism has been called Maxwell theory, and the four key equations of electromagnetism called Maxwell's laws or Maxwell's equations [3].

$$\nabla \times E = -J_m - \mu_o \frac{\partial H}{\partial t} \quad (2-14)$$

$$\nabla \cdot E = \frac{\rho_\epsilon}{\epsilon_o} \quad (2-15)$$

$$\nabla \times H = J_e + \varepsilon_o \frac{\partial E}{\partial t} \quad (2-16)$$

$$\nabla \cdot H = \frac{\rho_m}{\mu_o} \quad (2-17)$$

where : $E(r,t)$: Electric field vector

$H(r,t)$: Magnetic field vector

ε_o : Permittivity

μ_o : Permeability

ρ_e : Electric charge

J_e : Electric current density

ρ_m : Magnetic charge

J_m : Magnetic current density

Because the divergence of curl of any vector is equal to zero, one can obtain the current continuity equation, i.e.,

$$\nabla \cdot J_e + \frac{\partial \rho_e}{\partial t} = 0 \quad (2-18)$$

$$\nabla \cdot J_m + \frac{\partial \rho_m}{\partial t} = 0 \quad (2-19)$$

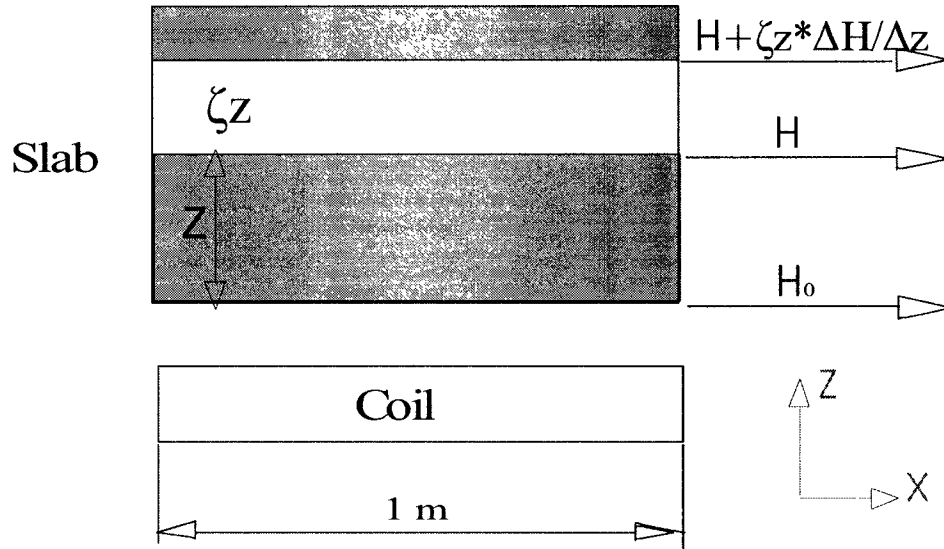


Figure 2-8. Magnetic flux and infinity conductor

Figure 2-8 shows a slab, with resistivity ρ , lying close to a sinusoidal varying field of amplitude H_0 . The pulsating H_0 will produce eddy current in the y direction inside the slab. The propagation of low frequency (up to 10 GHz) magnetic fields can be described by the diffusion equation [49]:

$$\nabla^2 H = \frac{\mu}{\rho} \frac{\partial H}{\partial t} \quad (2-20)$$

With $H_z = H_y = 0$ and by defining δ as the skin depth, $\delta^2 = 2\rho / \omega\mu$, equation (2-20) can be re-written as:

$$\frac{d^2 H_x}{dz^2} - 2j \left(\frac{1}{\delta} \right)^2 H_x = 0 \quad (2-21)$$

It is easy to get the final solution:

$$H_z(y) = H_{0m} \exp \left(-\frac{\sqrt{2j}}{\delta} z \right) \exp(j\omega t) \quad (2-22)$$

At a depth z inside the slab, the real part of H_x can be obtained as:

$$H_x(Z) = H_0 \exp\left(-\frac{1}{\delta}Z\right) \cos\left(\omega t - \frac{1}{\delta}Z\right) \quad (2-23)$$

The current density J at position z in the slab is given by Faraday's law of induction[50] [51]:

$$J(Z) = \omega\mu_0 H_x / \rho \quad (2-24)$$

The total loss per square meter of surface to a depth of ξ , can be defined by integrating J_z over the depth[11, 50, 51]:

$$P = \int_0^\xi \rho J^2 dz (\times 1 \times 1) \quad (2-25)$$

$$= -\frac{\mu_0^2 \omega^2 \xi^2 H_0^2}{\rho} \left[1 - \exp\left(-\frac{2\xi}{\delta}\right) \right] \quad (2-26)$$

The power dissipated at the magnetic skin depth, $\xi=\delta$, accounts for 96.2% of the total field energy. Figure 2-9 shows that when the frequency is of the order of MHz, the skin depth of pure iron is less than one millimeter, while that of skin tissue is several meters. Therefore, the field energy can be concentrated in a thin layer of iron, with little dissipation in the surrounding tissue.

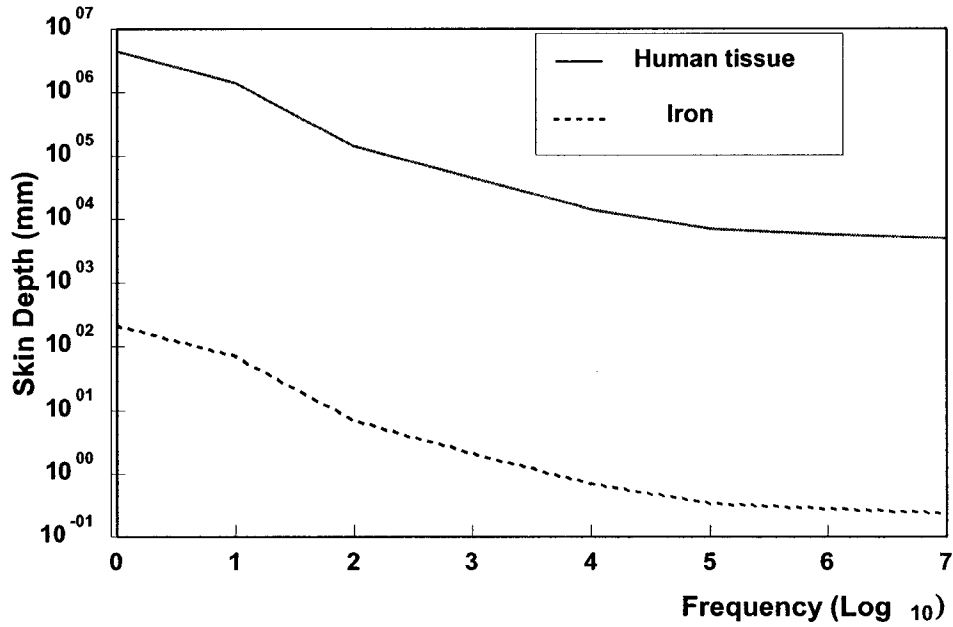


Figure 2-9. The skin depth of skin tissue and iron as a function of frequency. Resistivity is 2.53 and $1.84 \times 10^{-6} \Omega\text{m}$ for skin and iron. The relative permeability of tissue and iron is set at 1 and 300, respectively.

Bozorth [52], gave similar equations for the eddy current in sheets or cylinders after defining θ as:

$$\theta = 2\pi\delta\sqrt{\mu f / \rho} \quad (2-27)$$

When $\theta \gg 1$, the formulas yield:

$$P_e = W_e f = \frac{B^2}{4\mu} \cdot \frac{\Delta R}{2\pi f L_0} \cdot \frac{L_0}{L} = \frac{\pi^2 \delta^2 B^2 f^2}{6\rho} \text{ (Sheets)} \quad (2-28)$$

For cylinder and spheres of diameter d the corresponding expressions are:

$$W_e f = \frac{\pi^2 \delta^2 B^2 f^2}{16\rho} \text{ (Cylinders)} \quad (2-29)$$

$$W_e f = \frac{\pi^2 \delta^2 B^2 f^2}{20 \rho} \text{ (Spheres)} \quad (2-30)$$

When $\theta \ll 1$, the formulas yield:

$$P_e = W_e f = \frac{B'^2}{4\mu'} = \frac{\pi B'^2 f^{3/2} \delta}{2\mu'^{1/2} \rho^{1/2}} = \frac{B^2 \rho^{1/2} f^{1/2}}{8\pi\mu^{3/2} \delta} = \frac{H^2 (\mu \rho f)^{1/2}}{8\pi\delta} \quad (2-31)$$

for sheets and:

$$P_e = W_e f = \frac{B'^2}{4\mu'} = \frac{\pi B'^2 f^{3/2} \delta}{2\mu'^{1/2} \rho^{1/2}} = \frac{B^2 \rho^{1/2} f^{1/2}}{4\pi\mu^{3/2} d} = \frac{H^2 (\mu \rho f)^{1/2}}{4\pi\delta} \quad (2-32)$$

for cylinders.

2.6 Comparing Heating Capacity for Various Mechanisms

The heat generation capacity of magnetic particles is usually quoted in the terms of SAR in units of W/g . In the above sections we give four main induced heating mechanisms, covering the size range from nanometer to micrometer. We neglect the magnetic resonance, which usually requires an excitation frequency into the GHz range [53]. The total loss in a conductor media is [45, 54]:

$$P_{total} = P_h + P_e + P_r \quad (2-33)$$

where P_h , P_e and P_r stand for hysteresis, eddy current, effective Néel and Brownian losses, respectively. Thus the total loss per unit frequency can be expressed as [55]:

$$P_{total} = \frac{\beta_1 \mu_0 H^2}{\tau_e} + \beta_2 \frac{\mu_0^2 H^2 f}{\rho} + \frac{\beta_3 (mH)^2}{kT\tau_r} \quad (2-34)$$

where τ_h and τ_r stand for hysteresis and effective relaxation time, respectively. As we mentioned before, the coercivity of most ferromagnetic materials of sub-micrometer requires field strength of 100kA/m or more to reach a fully saturated status. Thus only a portion of hysteresis loops can be utilized given the operational physical constrain of around 15kA/m field amplitude [43]. Thus hysteresis heating will give rise to low SARs of ferromagnetic particle. The Superparamagnetic particles in nanometers would be a proper candidate for hyperthermia. In vivo, these could generate much more heat compared to conventional ferro/ferri magnetic particles exhibiting hysteresis losses.

According to Formula 2-34, the heating capacity of eddy current is linearly dependent on frequency and conductivity. Most ferromagnetic oxides have a very high resistivity of over $10^8 \Omega m$. Thus traditional clinical hyperthermia application utilizing ferro oxides will see minimal eddy current thermal dissipation effect. Actually, the eddy current will excite more energy dissipation in human tissue than in ferro oxide particles as the former has a resistivity of less than $20 \Omega m$. Obviously, the eddy current will provide the highest level of heating capacity among the above mechanisms by utilizing ferro conductor particles, e.g., iron with an electrical resistivity of $10^{-5} \sim 10^{-6} \Omega m$ or less.

Given that the energy source is concentrated within a small spherical with radius R and surrounded by a homogeneous medium with thermal conductivity of λ , a mass density of σ , and specific heat capability of c . The equilibrium temperature (i.e., $t \rightarrow \infty$), as a function of the distance r from the center and counted from the starting temperature before heating is given by [43]:

$$\Delta T = P \cdot [R^2 - r^2 + 2R^2 \lambda_1 / \lambda_2] / (6\lambda_2) \quad (r < R) \quad (2-35)$$

$$\Delta T = PR^3 / (3\lambda_2 r) \quad (r > R) \quad (2-36)$$

Thus a micrometers or even large metal particle will be several orders more efficient in hyperthermia applications than nanometer particles. Theoretically, the size of the particle, utilizing eddy current loss, can be of sub-millimeter, a size comparable to the magnetic skin effect depth. That the larger micrometer size particle can be used in the eddy current energy dissipation will bring new applications otherwise hard to achieve with the traditional nanometer sized particles.

2.7 Energy, Thermal, and Solid Modeling

The incurrent time-average surface eddy current loss in a conductor can be calculated by the following formula [56]:

$$Q^j = \text{Re} \left(\int [\rho] \{J_{ii}\} \{J_{ii}\}^* dv \right) \quad (2-37)$$

where Q^j , $[\rho]$, $\{J_{ii}\}$ and $\{J_{ii}\}^*$ are the Joule heat per unit volume, resistivity, current density and virtual current density at the integration point, respectively.

The thermal heating per unit volume will be used to calculate the temperature gradient inside the fibre. Consider a general temperature distribution in a three-dimensional body. Inside the body, the temperature field is space- and time-dependent [57].

$$T = T(x, y, z, t)$$

$$\nabla T \equiv i \frac{\partial T}{\partial x} + j \frac{\partial T}{\partial y} + k \frac{\partial T}{\partial z} \quad (2-38)$$

Fourier's law summarizes the heat flux \vec{q} gradient as:

$$\vec{q} = -k\nabla T \quad (2-39)$$

or

$$q_x = -k \frac{\partial T}{\partial x} \quad q_y = -k \frac{\partial T}{\partial y} \quad q_z = -k \frac{\partial T}{\partial z}$$

The thermal conductivity k depends on position and temperature in the object. But in most materials, the thermal conductivity is nearly homogeneous. Under the condition that the temperature distribution is approximately uniform, e.g. the fibre in our model, the thermal conductivity can be considered a constant. The first law of thermodynamic for a closed system takes the form of [57]:

$$Q = -\frac{dU}{dt} \quad (2-40)$$

where Q , and dU / dt are the heat transfer rate, and the change of internal thermal energy rate, respectively. Considering the heat generated within the region R, the heat flows out and generates in a surface dS can be expressed as:

$$Q_{out} = \int_R (-k\nabla T) \cdot (\vec{n}dS) + \int_R \dot{q} dR \quad (2-39)$$

$$\frac{dU}{dt} = \int_R \left(\rho c \frac{\partial T}{\partial t} \right) dR \quad (2-40)$$

Formula 2-38 can be rewritten as:

$$\int_S (-k\nabla T) \cdot (\vec{n}dS) = \int_R \left[\rho c \frac{\partial T}{\partial t} - \dot{q} \right] dR \quad (2-41)$$

The Gauss's theorem will enable to convert a surface integral into a volume integral as:

$$\int_S \vec{A} \cdot \vec{n} dS = \int_R \nabla \cdot \vec{A} dR$$

The formula 2-41 can be expressed as:

$$\int_R \left(\nabla \cdot k \nabla T - \rho c \frac{\partial T}{\partial t} + \dot{q} \right) dR = 0$$

Since the region R is arbitrary, the integrand must vanish identically. Therefore, we get the heat diffusion equation in three dimensions [57]:

$$\nabla \cdot k \nabla T + \dot{q} = \rho c \frac{\partial T}{\partial t} \quad (2-42)$$

The assumption for the above equation is that: first, the object is an incompressible medium; second, no convection exists at the boundary. In our model, the energy loss occurs at the human skin-air interface. As the heating interval in the model is of the order of several milliseconds, thermal radiation and convection due to body fluid circulation is neglected.

Convection and radiation are the main modes of energy loss occurring at the boundary interface. Heat transfer rate due to radiation and convection can be written as: [49].

$$P_r = \frac{5.67}{10^8} \varepsilon [T^4 - T_0^4] \quad (2-43)$$

$$P_c = 1.54 * (\Delta T)^{4/3} \quad (2-44)$$

where P_r and P_c are radiation and convection losses, respectively; ε is the emissivity coefficient of the surface; and ΔT is temperature rise above ambient in Kelvin.

From Figure 2-11, thermal radiation will transfer several times more heat than convection at the interface when the temperature variation is within a few degrees

Celsius above ambient. Thus we choose convection as the sole mode of heat transfer and use an ambient temperature of $37^{\circ}C$.

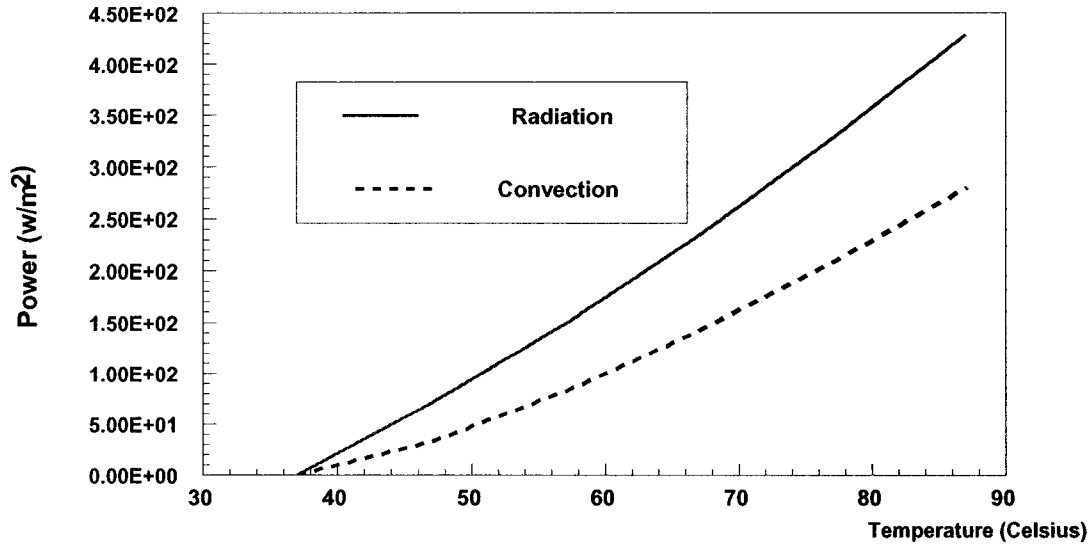


Figure 2-11. Energy dissipation due to convection and radiation. Emissivity is 0.98. Ambient temperature is $37^{\circ}C$ [58].

The fibre consists of bi-layers of iron and polymer. During heating, the polymer will be pulled into tension by the iron, which in turn will be restrained by the polymer and is under compression. These two forces produce a moment that will cause the composite fibre to bend into a uniform arc. The model of double layer cantilever was developed by using the models of Judy [59] and Timoshenko [60]. Combining the above two methods, Edmon[61] gave a model to compute the radius of the cantilever due to thermal and evenly distributed surface forces:

$$\alpha_1 \Delta T + \frac{\sigma_1}{E_1} + \frac{P_1}{E_1 t_1 b} + \frac{t_1}{2\rho_1} = \alpha_2 \Delta T + \frac{\sigma_2}{E_2} - \frac{P_2}{E_2 t_2 b} - \frac{t_2}{2\rho_2} \quad (2-45)$$

where ρ_1 and ρ_2 are the curvatures at initial and final temperatures, respectively. ΔT is the temperature variation. $\alpha_i (i=1,2)$ is the thermal expansion coefficient of polymer and iron in the temperature range. $E_i (i=1,2)$ is the modulus of elasticity of

the two components, and t_i ($i=1,2$) is the corresponding layer thickness. P_i ($i=1,2$) and b are the distributed surface force and cantilever width. σ_i ($i=1,2$) is the residual stress within the two components. When P_i is zero, the Formula 2-45 can be expressed as:

$$\frac{1}{\rho} = \frac{(\alpha_2 - \alpha_1)\Delta T - \frac{\sigma_1}{E_1} + \frac{\sigma_2}{E_2}}{\frac{a_1 + a_2}{2} + 2\left(\frac{E_1 a_1^3 - E_2 a_2^3}{12}\right)\left(\frac{1}{E_1 a_1} - \frac{1}{E_2 a_2}\right)} \quad (2-46)$$

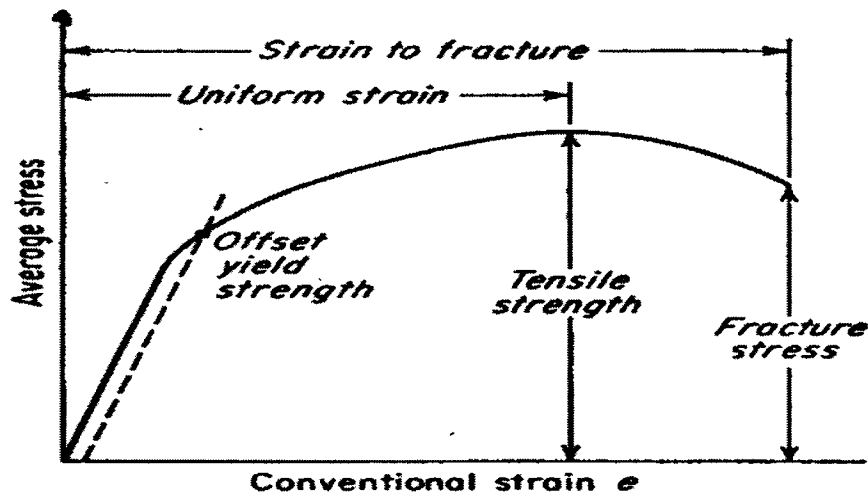


Figure 2-12. Stress & strain relation of plastic engineering material.

Most engineering materials exhibit complicated stress-strain relationship as shown in Figure 2-12. The plastic behavior, characterized by nonrecoverable strain, begins when stress exceed the material's yield point. Plasticity is a nonconservative, path-dependent phenomenon. The sequence in which loads are applied and in which plastic responses occur affects the final solution results. For large strain analysis, a bilinear Isotropic hardening using Von Mises yield criteria coupled is preferred[56].

Chapter 3

FEM Multiphysics Model

3.1 Coupled Electromagnetic-thermal Analysis

The magnetic saturation value of ferromagnetic material is nonlinear magnetic flux intensity dependent. The magnetic saturation value of pure iron at 0k is maximum of 2 Tesla, while it is near zero at a Curie temperature of 1043K [62]. For iron, thermal conductivity and electrical resistivity are both temperature dependant.

There are two approaches to the solution of the multi-physics nonlinear problems. Either an electromagnetic solver performs co-simulation of both electrical and thermal subsystems, or an electromagnetic solver and a thermal solver couple to complete relaxation iteration. We prefer to use the relaxation method for that the electromagnetic and thermal models can differ in their numerical domain size. Figure 2 shows such an iteration flow.

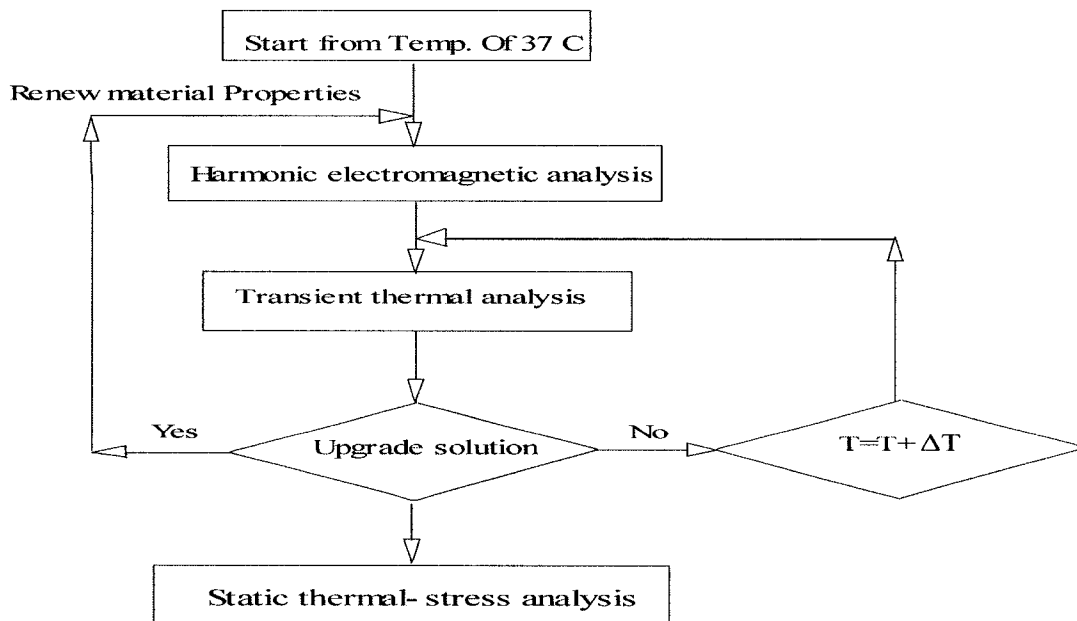


Figure 3-1. The relaxation iteration flow.

ANSYS® 8.0 Multiphysics™, a popular finite element method software, was used to model the electromagnetic-thermal multiphysics process. ANSYS® 8.0 Multiphysics™ provides coupled physics tools combining structural, thermal, CFD, acoustic and electromagnetic simulation. ANSYS® 8.0 Multiphysics™ provides two approaches for the Multiphysics domain problems, a coupled analysis and multi-field solver.

A coupled-field analysis involves the interaction between two or more disciplines of physics. In our case, it is an electromagnetic-thermal-structural analysis. Two distinct methods, sequential and direct, can be employed in the coupled-field analysis in ANSYS® 8.0 Multiphysics™. In a sequential coupled method, one will use results from one analysis as the input for another analysis to couple the two fields. In this specific model, the induced energy from the electromagnetic field is applied as “body force” in the subsequent thermal analysis. Then the temperature distributions are input in the solid stress analysis. Physics files from both electromagnetic and thermal analysis are used to perform coupled-field analysis. These physics files are individually created. Harmonic electromagnetic and thermal solutions proceed in a sequential manner. First the harmonic electromagnetic physics file is read to configure the database, a solution is performed, then the thermal physics field is read into the database, coupled-field loads are transferred, and the second physics is solved. The results from the thermal analysis will then trigger the configuring adjustment in the electromagnetic physics files. Coupling occurs by issuing commands to read the coupled load terms from one physics to another across a node-node similar mesh interface [56].

“The direct method usually involves just one analysis that uses a coupled-field element type containing all necessary degrees of freedom. Coupling is handled by calculating element matrices or element load vectors that contain all necessary terms. Direct coupling is advantageous when the coupled-field interaction is highly nonlinear and is best solved in a single solution using a coupled formulation. Examples of direct coupling include piezoelectric analysis; conjugate heat transfer with fluid flow, and circuit-electromagnetic analysis. Elements are specifically formulated to solve these coupled-field interactions directly” [56] .

The multifield solver is also available since ANSYS® 8.0 for almost all of the coupled problems. “The multifield solver is an automated tool for solving sequentially coupled field problems. It is a superset of the Fluid Solid Interaction solver and is an alternative for the physics file based procedure. It provides a robust, accurate, and easy to use tool for solving sequentially coupled physics problems. The solver is built on the premise that each physics is created as a field with an independent solid model and mesh. Surfaces or volumes are identified for coupled load transfer. Coupled loads are automatically transferred across dissimilar meshes by the solver. The solver is applicable to static, harmonic, and transient analysis, depending on the physics requirements. Any number of fields may be solved in a sequential (staggered) manner. The stagger solver has three nested loops: time, stagger and field” [56]. The figure 3-2 shows the implementation of stagger loop.

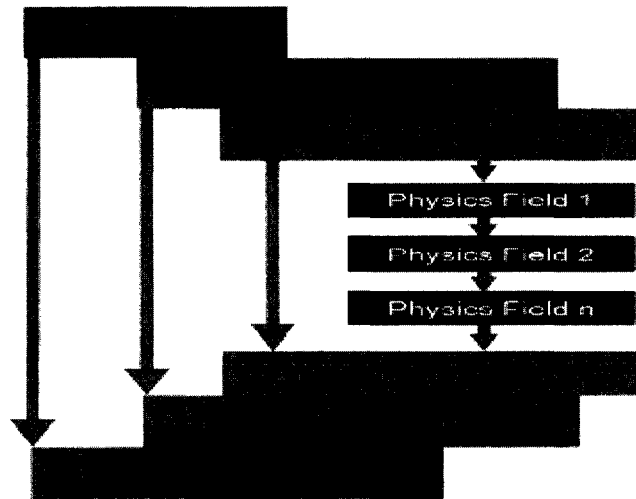


Figure 3-2 Flow diagram showing implementation of a multi-field solver [56].

The ANSYS® 8.0 Multiphysics™ does not provide a direct coupling element for the magnetic-thermal interface. In our model, the air adjacent to the chest is modeled in the electromagnetic analysis but will be removed in the thermal analysis. So, a sequential coupled analysis is the best choice. The disadvantage of the sequential analysis is that the time span for the initial several iterative steps will be reduced to a certain amount to achieve a smooth temperature rise curve. But the small time step will trigger a long processing time and require more storage capacities for computation. The solution is recursive iteration with variable time step. As a result, we can create very fine steps in the initial energy absorption process and use large time span for the near-balance-temperature stage. This gives the model advantages of both accuracy and efficiency.

In the fibre thermal transfer model, the initial and the final time step ΔT is 10^{-5} and 10^{-4} seconds, respectively. There are 10 iterations in approximately 3×10^{-3} seconds of simulation.

3.2 Model Overview

This study concentrates on the bending deformation of a fibre by the thermal energies of induced eddy current inside the imbedded magnetic particles. The models are shown in the figure 3-3 and 3-4. This research introduces a coupled electromagnetic-thermal model to simulate the nonlinear characteristics of material properties.

The fibre has a cross-section of 400x220 nm and its length is 20 μ m (Figure 3-3). It is floating inside an alveolar duct of lung. The length to height ratio of the fibre is around 45. The main body of the fibre is polyethylene, while the middle upper surface and embedded intrusions are epitaxial pure iron. The top thin layer of iron, which is utilized for its mechanical properties, creates a differentiation in thermal expansion and elastic modulus from the polymer. The cross-section and distribution of the iron along the Z-axis, as well as the cross section of the fibre are designed to achieve an uniform heating of the fibre.

The iron shell and iron particles are of thickness 20nm and 200nm, respectively, both being greater than 2.5 nm, the single domain size of iron[63]. Energy losses due to hysteresis and eddy current are predominant in the iron. Due to the low electrical resistivities, the hysteresis losses of iron are a small fraction of those of eddy currents. Therefore, in our model we will only compute the thermal energy generated from eddy currents.

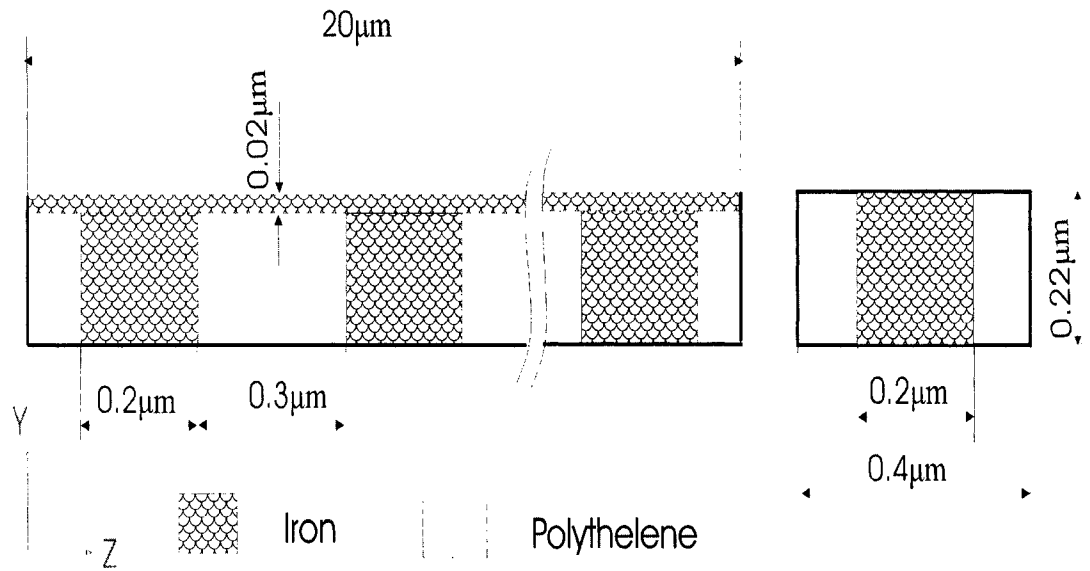


Figure 3-3: Iron embedded fibre and cross section

ANSYS® 8.0 Multiphysics™, is used to model the electromagnetic-thermal process. The target fibre is placed in an evenly distributed magnetic field (Figure 3-4). As the embedded iron studs are cubic, a 2-D model can be used to approximate the 3-D geometry, with the assumption that the eddy-current flows only in the X direction. A 2-D induced heat model is also assumed. The model is amenable to several other assumptions. First the top iron shell surface of the fibre will remain perpendicular to the magnetic flux. Second, the individual embedded iron studs are approximated as infinite in length. Third, the iron studs and sheet are perfectly electrically insulated. Iron nonlinear temperature dependant resistivity and B-H curves are shown in the appendix[56, 64-66]. As the final temperature in the simulation is approximately $80^{\circ}C$, far below the Curie temperature, we assume that the B-H curve remains unchanged during the temperature rise.

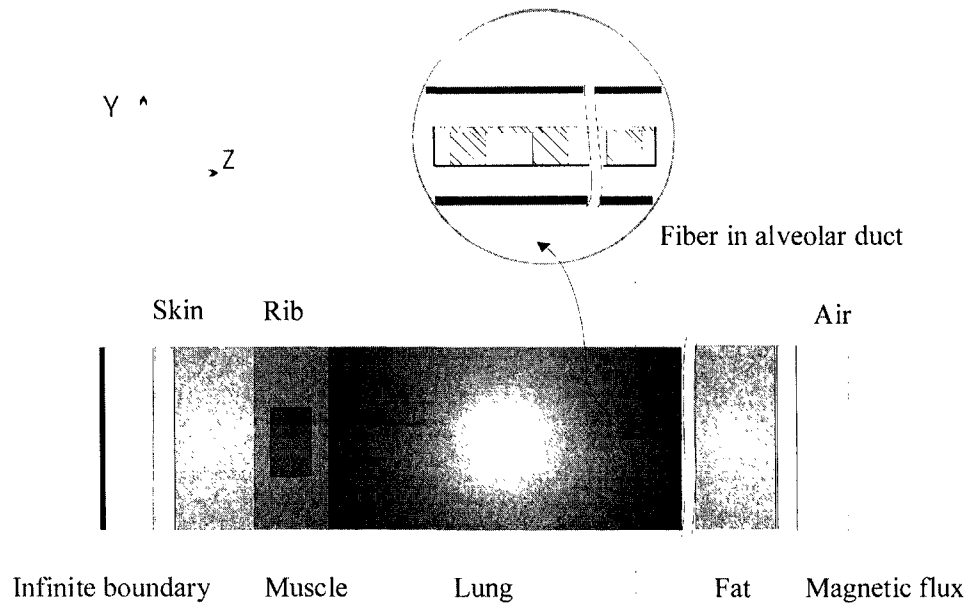


Figure 3-4. Cross-sections of human torso placed in a magnetic field. The fibre is airborne inside the alveolar duct of lung.

3.3 Material Properties

In the simulation, we set all the permeability of human tissue to be 1, while those of electrical resistivity and other parameters shown in Table 3-1 are from literature survey [7, 67].

Table 3-1: Material properties[7, 67]

	Units	Air	Tissue	Iron	Polyethylene
Relative Permeability		1	1	~250	1
Resistivity	Ωm	~	1.25~14	$3 \sim 6.5 \times 10^{-6}$	10^{17}
Conductivity	$W / m^{\circ} K$	0.03	0.5	60.4	30
Specific Heat	$J / (kg)^{\circ} K$	1.2	1256-3662	1500	1720
Density	Kg / m^3	1.2	1058~1810	7800	940
Thermal expansion	$M / m^{\circ} K$			16	150
Elastic Modulus	$Kg / (m)(s)^2$			193×10^9	4×10^9
Yield Stress	MPa			300	6
Passion Ratio				.3	0.42
Melting Point	$^{\circ} C$			700	135

The resistivity of metal is temperature dependent. According to the Matheissen's rule [68]:

$$\rho(T) = \rho_0 + \rho_{ph}(T) + \rho_{mag}(T) \quad (3-1)$$

where ρ_0 is the residual resistivity, $\rho_{ph}(T)$ is the contribution from electron-phonon interaction, and $\rho_{mag}(T)$ is the contribution from electron-spin wave scattering. $\rho_{ph}(T)$ and $\rho_{mag}(T)$ dominate at different temperatures.

In the low temperature domain, the resistivity of magnetically ordered materials arises due to electron-electron scattering, electron-spin wave scattering and electron-phonon scattering [69]. Mannari [70] showed that, at low temperature, the contribution from the electron-phonon scattering is found to be small compared with the other two contributions. The temperature dependence of resistivity due to the electron-electron and electron-spin wave scattering follow a T^2 behavior, where T is in the range of $\sim 50\text{K}$ [65, 71-73].

$$\rho(T) = \rho_1 + AT^2 \quad (3-2)$$

The value of A reflects either electron-electron scattering or electron-spin scattering or both play a significant role in the determination of resistivity [74]. The value of A should be small (of the order of $2.5 \times 10^{-5} \mu\Omega\text{cmK}^{-2}$) when the electron-electron interaction dominates, which is the case of pure metal. The value of A will be quite high (of the order $4 \sim 5 \times 10^{-3} \mu\Omega\text{cmK}^{-2}$), in the case of compound alloys [69].

The high temperature domain usually refers to 100-400K. In this domain, the electron-phonon interaction is found to be dominant, which gives a near linear increase in the resistivity with temperature [75]. This relation can be rewritten in a more general forms as [69]:

$$\rho(T) = A + BT - DT^3 \quad (3-3)$$

As D is of the order 10^{-7} , so in the 100~400K range, the resistivity curve is still positive.

The iron particles in the model are around 200nm in size. The resistivity of the iron particle is not uniform through the dimension. The small iron particles are usually covered by several nm thickness of Fe_2O_3 . The resistivity of an iron particle, of the size less than micrometer, can be described by conduction theory in which large conducting regions are separated by small insulating barriers [76]. Zhang measured a resistivity of 10^4 of crystalline Fe of about 100nm in diameter. Nanocrystalline Fe (100nm to 200nm) under quasi hydrostatic pressure of 6 GPa shows a 55% higher resistivity than polycrystalline Fe [66]. This increasing resistivity of the nanocrystalline metals is due to additional electron scattering on the grain boundaries since the grain boundary density there is much higher compared with the polycrystalline solids.

We speculate that the 20nm thick iron on the fibre surface would be of great variation in composition. However, in our simulation, we will assume uniformity of composition both in this thin layer and studs. The thin layer of iron oxide at the

surface provides a perfect electrical insulation for the iron in the core. An assumed temperature dependent resistivity of the iron is showed in Figure 3-5.

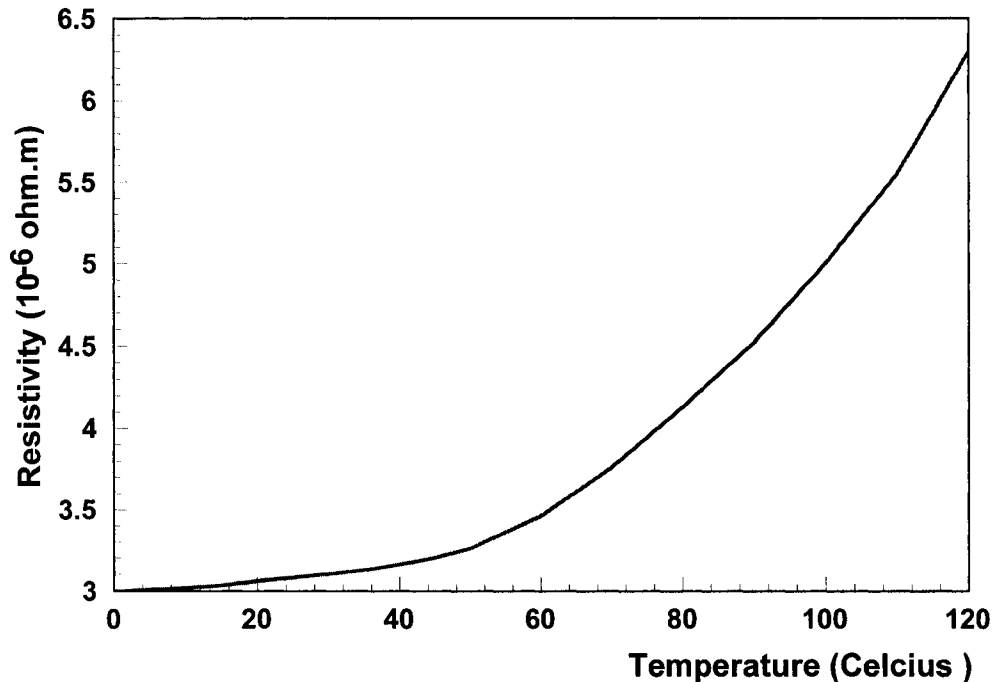


Figure 3-5: Micron size iron particle temperature dependent resistivity

Barton [77] measured the iron permeability in a magnetic field with oscillation frequency between 300-1300MHz. He used iron wire with a resistivity of $3.2 \times 10^{-7} \Omega m$ and found the relative permeability range between 30 to 9. Wait [78] showed the permeability of iron to be around 120 at 1.0MHz field. In our simulations, we assume a B-H curve as in Figure 3-6, with a permeability value of ~ 250 . The relative permeability of iron is almost independent of the energy dissipation rate in the iron, while a large relative permeability value of tissue will definitely increase its energy dissipation.

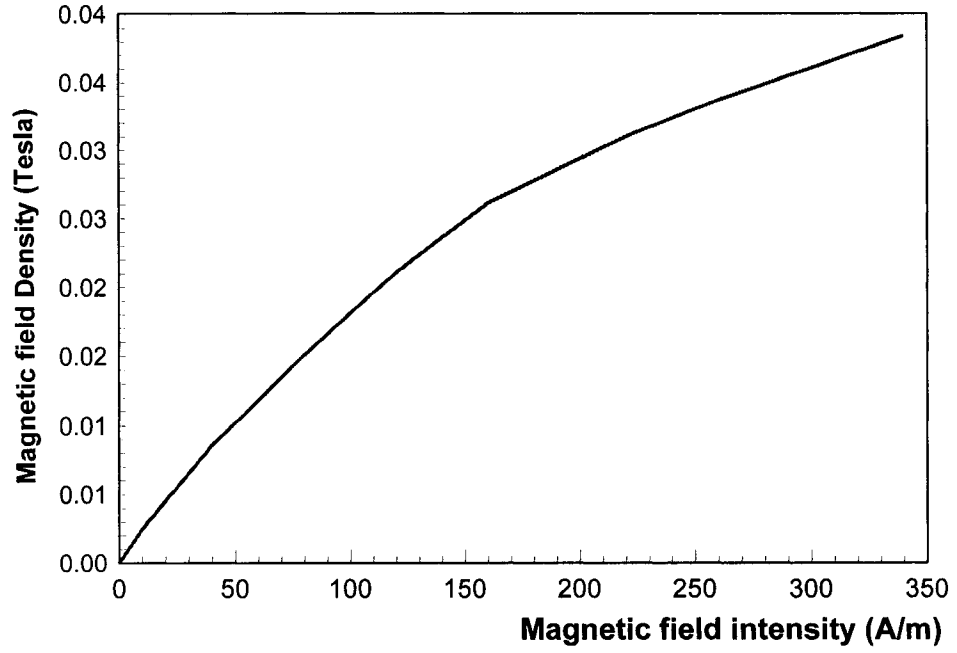


Figure 3-6: Iron B-H curve in 1MHz field

Chapter 4

FEM Simulation

4-1 2-D Modeling

The ANSYS® 8.0 Multiphysics™ provides 2-D and 3-D simulation capabilities of electromagnetic related problems. The 2-D elements can simulate none-linear material properties, while 3-D elements are only suitable for linear material property [56].

The geometry of the 2-D simulation follows the theoretical assumptions. The 2-D model is placed in a magnetic field with uniform magnetic flux. A 2-D FEM model is shown in Figure 4-1.

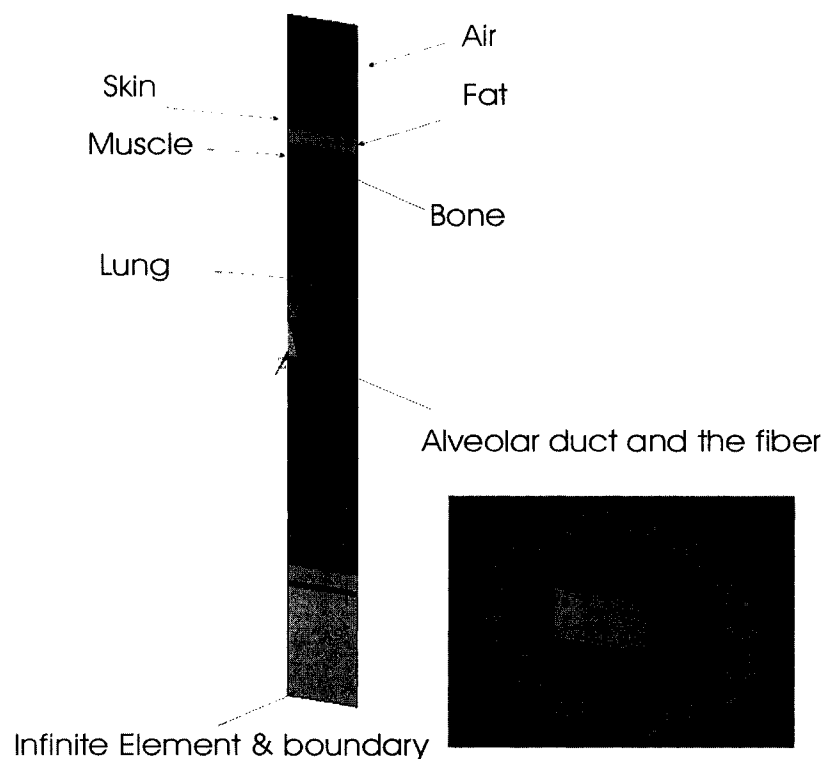


Figure 4-1 Model of 2-D simulation

In ANSYS, a 2-D plain element 13 (Plane 13) is chosen to build the electromagnetic model. PLANE13 has a 2-D magnetic, thermal, electrical, piezoelectric, and structural field capability with limited coupling between the fields. PLANE13 is defined by four nodes with up to four degrees of freedom per node. The element has nonlinear magnetic capability for modeling B-H curves or permanent magnet demagnetization curves. INFIN110 is used to model the open boundary of the 2-D model. A single layer of elements is used to represent the exterior sub-domain of semi-infinite extent. This element has 2-D (planar and axisymmetric) magnetic potential capability. The largest meshing size of the fibre and tissue is 0.02x0.02 micron and 4x8 mm, respectively. These sizes are far smaller than the corresponding skin depths shown in figure 2-10. There are a total of 21814 nodes in 35786 elements. Convergence tests show that varying the number of nodes from a total of 5873 to 532498 (corresponding to 3706 to 867122 elements) results in less than a 0.1% difference in induced energy density indicating the sufficiency of our grid resolution. We set the permeability of human tissue to be 1. Magnetic flux intensity and frequency are 2.6kA/m and 1.0MHz, respectively. The magnetic flux intensity is applied on the upper air surface.

Figure 4-2 and 4-3 show the distribution of magnetic flux with and without the infinite element. The magnetic field intensity near the skin surface in Figure 4-3 is approximately half of the applied oscillation magnetic flux. But the magnetic flux intensity in Figure 4-2 seems distorted. These two magnetic flux intensity give two

energy dissipation densities with the latter being a factor of 4 bigger than the former. By using equation in Chapter 2 from 2-26 to 2-34, it is found that Figure 4-2 with infinite element gives the approximate energy density level.

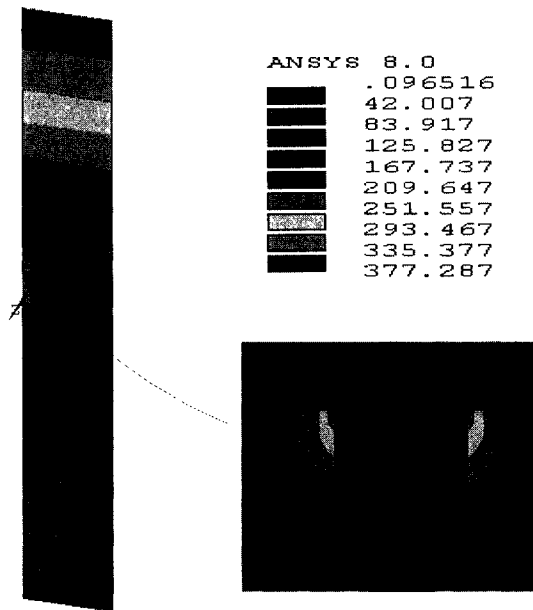


Figure 4-2. The magnetic intensity of the cross-section with infinite element, Magnetic flux intensity and frequency are 2.6kA/m and 1.0MHz

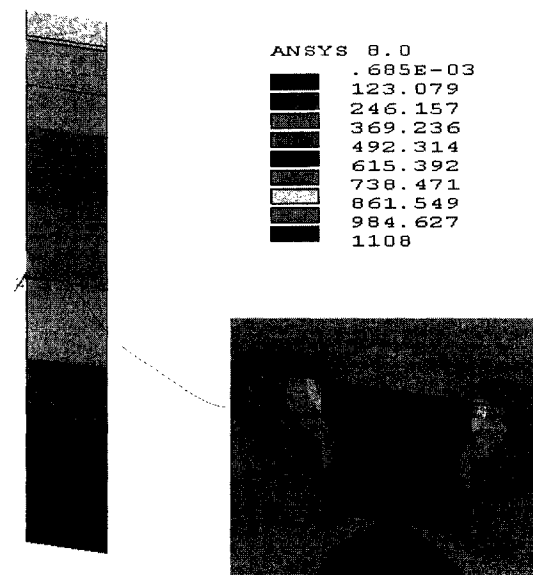


Figure 4-3. The magnetic intensity of the cross-section without infinite element. Parameters are the same as Figure 4-2

Table 4-1 lists the results of energy density given by the simulation. Figure 4-4(1) shows the induced heat power density of the iron, polyethylene and surrounding human tissues. The data shows an up to 7 order of magnitude difference in unit energy density between iron and human tissue. Due to the high resistivity of polyethylene, its energy absorption rate is minimal. These are predicted by equation (2-26).

Table 4-1 Energy depositions rate of the tissues Units: $W, W/m^3$

	IRON	POLYMER	SKIN	FAT	MUSCLE	BONE	LUNG
Power (actual)	1.61	1.99E-22	5573	3706	9218	1665	87441
Power density	8.40E+13	4.98E-09	1.96E+07	1.20E+07	2.10E+07	1.80E+08	1.36E+07

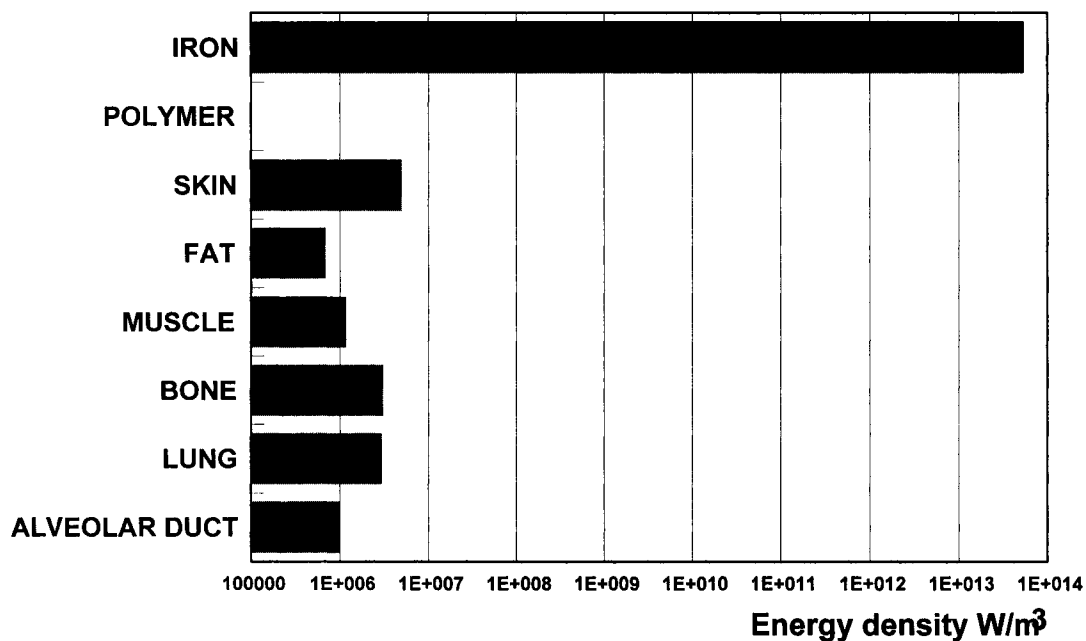


Figure 4-4(1). Induced heat power of embedded iron studs and human tissues at 1.0MHz, 2.6kA/m field.

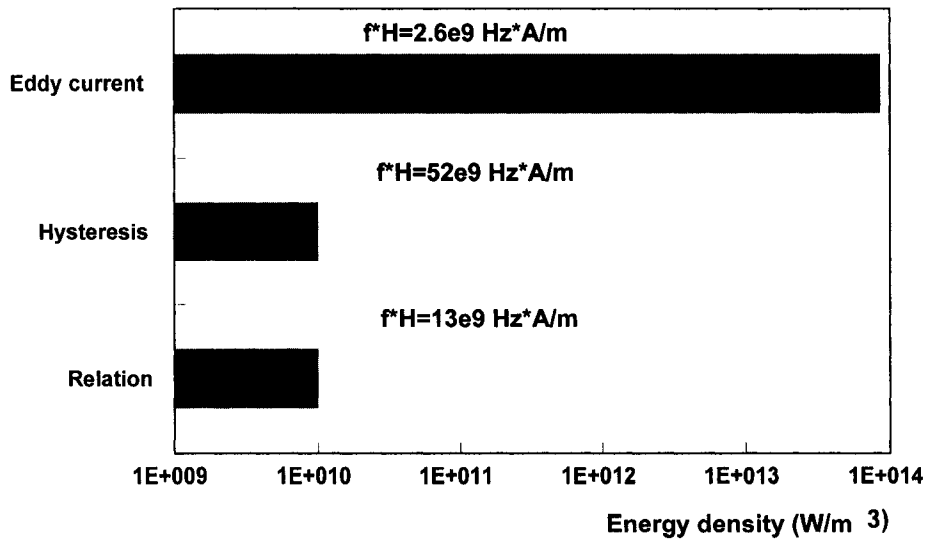


Figure 4-4(2) Comparing of energy density in various mechanisms. Hysteresis and relaxation data are from Hergt [43].

Figure 4-4(2) shows the energy dissipation of eddy current is over three orders higher than that of theoretical hysteresis and relaxation losses. Especially, the $H \cdot f$ product is much lower in the eddy current settings when compared to the other two.

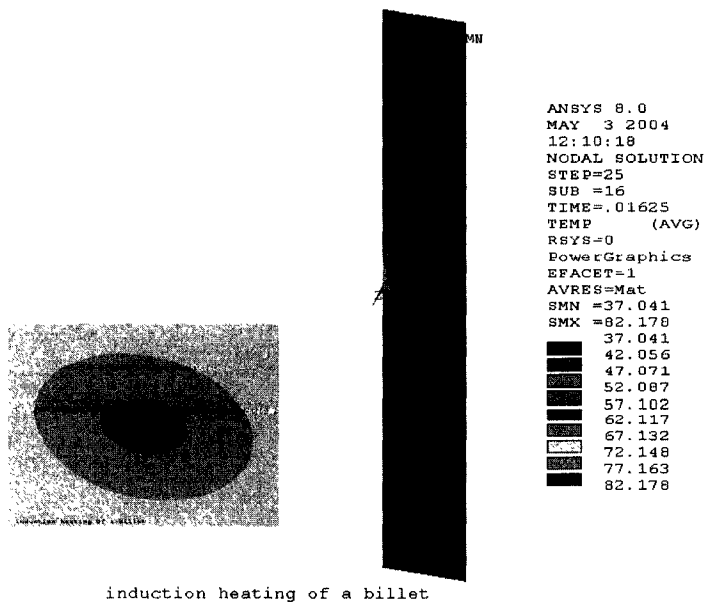


Figure 4-5 Temperature distribution of the tissues and fibre

Figure 4-5 shows the temperature distribution in the model after 0.002 seconds of heating. The highest temperature area is approximately the fibre cross-section. The air within a radius of 100 μm around the fibre is heated up to approximately 47°C . Figure 4-6 shows the temperature distribution in the fibre cross-section. The temperature distribution in the fibre cross-section shows a 0.5 Celsius spatial variation. This contributes to a low thermal conductivity of the polymer and the surrounding air. Figure 4-7 shows the fibre temperature rises very quickly vs. those of the human tissues. The temperature rise in human tissues falls in the same pattern and is less than 0.07°C at the simulation end. The temperature rise patterns meet our theoretical expectations.

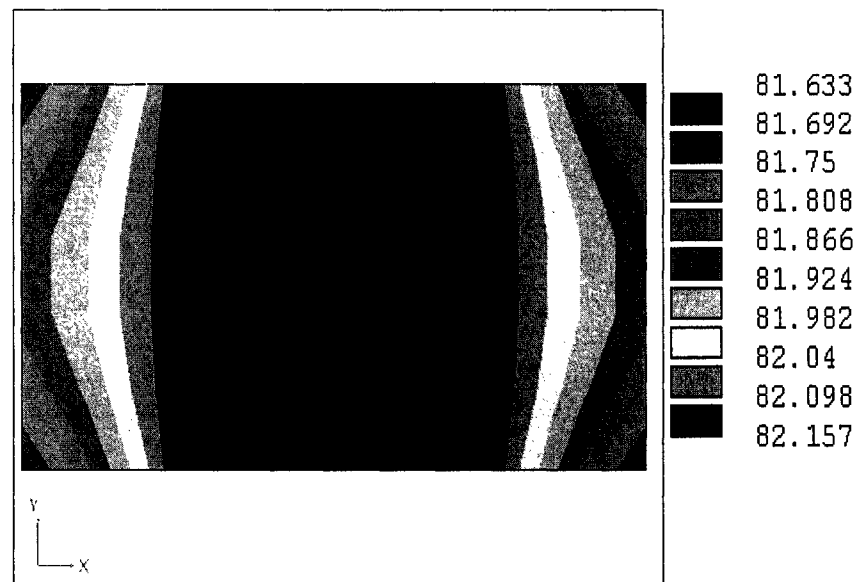


Figure 4-6 The temperature distribution of fibre section after 0.002 second of heating.

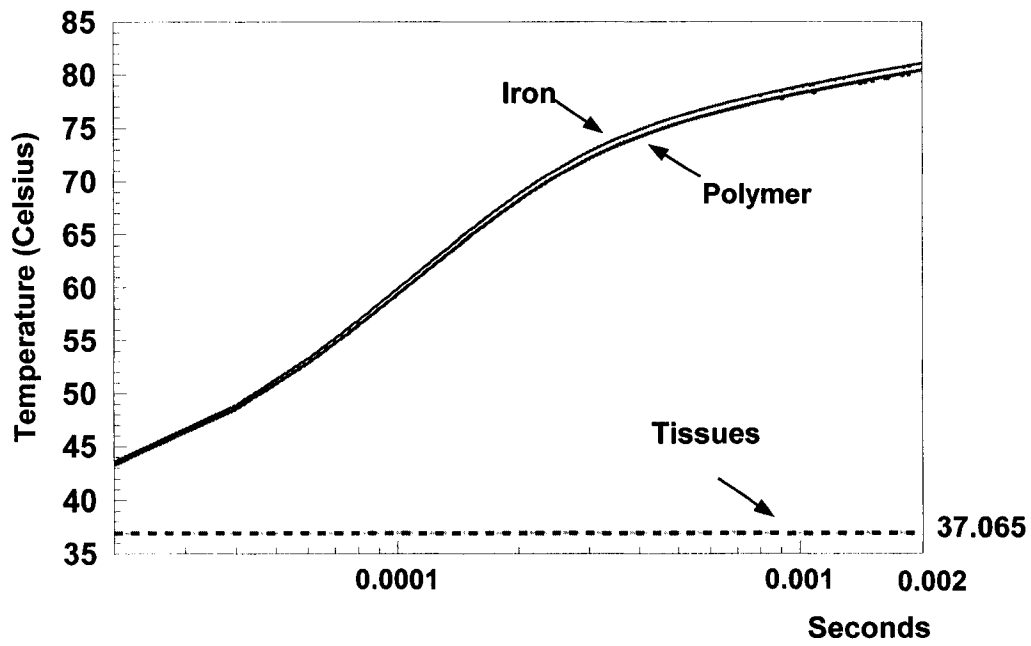


Figure 4-7 Temperature rise vs. time due to magnetically induced heating in magnetic field of 2.6kA/m and 1.0MHz. Heating time is 0.002 seconds.

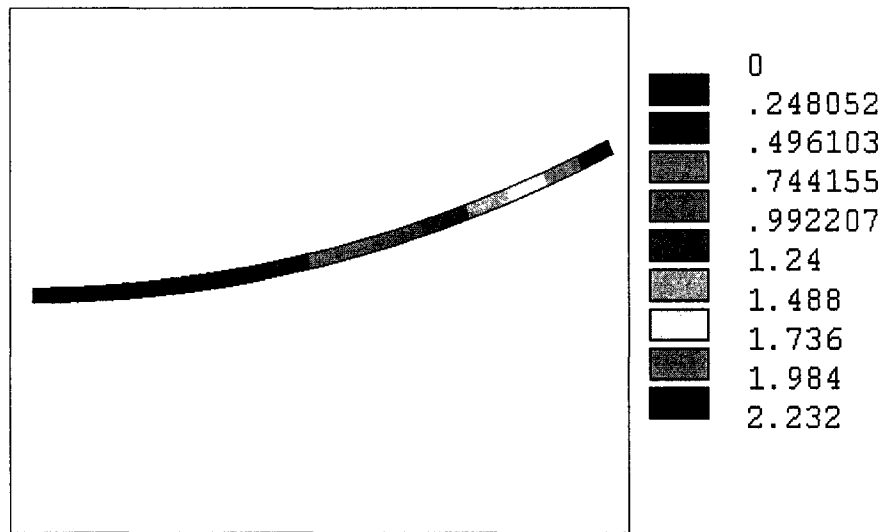


Figure 4-8. Thermal bending of the fibre at 80°C, units in µm.

The electromagnetic-thermal simulation predicts a nearly uniform temperature distribution in the fibre cross-section. In the model, the separation between two iron studs is $0.3\mu\text{m}$, while the side wall thickness is $0.2\mu\text{m}$. From figure 8 we find the temperature curve is fairly flat around 80°C . Thus it is reasonable to assume the temperature distribution is independent of the longitudinal direction in the mechanical deformation analysis. Structure 42 element is employed to construct a 3D model, of half of the fibre, fully constrained at the middle plane. Isotropic strain hardening models were employed in constructing both materials, which use the Von Mises stress to define the onset of yielding. The yielding stress for iron and polyethylene is set at 300 MPa and 6 MPa, respectively [67]. Another assumption is the residual stress inside the fibre vanishes at 25°C . Figure 4-8 shows the tip displacement of the fibre as a result of a uniform temperature of 80°C . As the melting temperature of polyethylene is around 135°C , over heating the fibre, say over 80°C , may cause the fibre to creep.

4-2 3-D Modeling

A 3-D simulation is important for two reasons. First in the 2-D simulation, we assume the eddy currents only exist in one direction. Second, the finite length of iron particles are infinite in length. A 3-D simulation will verify the above assumptions. The nodal based 3-D simulation in ANSYS® 8.0 Multiphysics™ is only suitable for linear material properties. Strictly, the 3-D nodal based simulation is not applicable for the above electromagnetic-thermal coupled analysis.

However, the temperature dependent resistivity can be assumed approximately

constant as the temperature rise in the simulation is limited to $80^{\circ}C$. According to equation 2-26, the energy deposition is approximately independent of iron permeability because of the large difference of magnetic skin depth and the iron geometry size. The material permeability can also be fixed as the outside magnetic field intensity is fixed. Figure 4-9 shows the 3-D model of the fibre. The cross-section is 200×400 nm with a $20 \mu\text{m}$ length. There are 40 iron particles ($200 \times 200 \times 200$ nm) evenly distributed along the longitudinal axle (Figure 4-10).

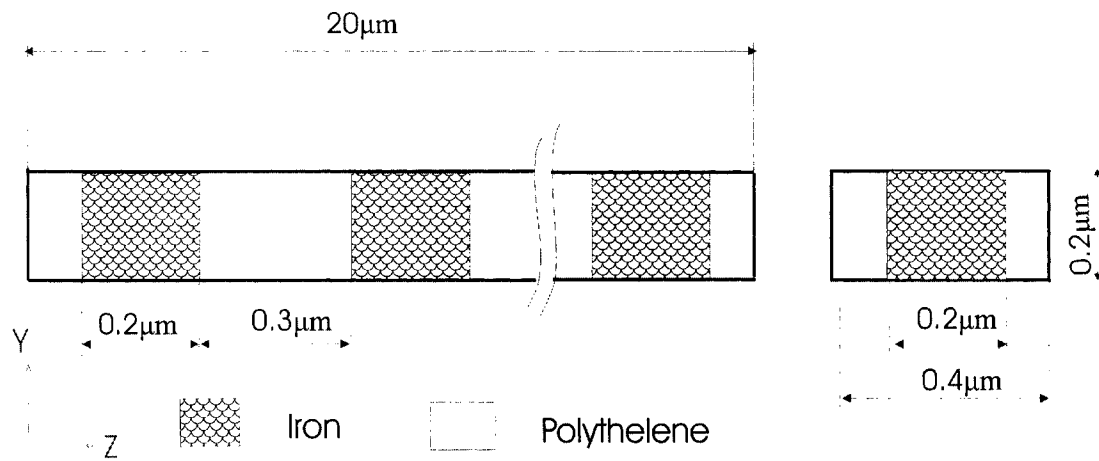


Figure 4-9 Fibre model used in 3-D FEM analysis

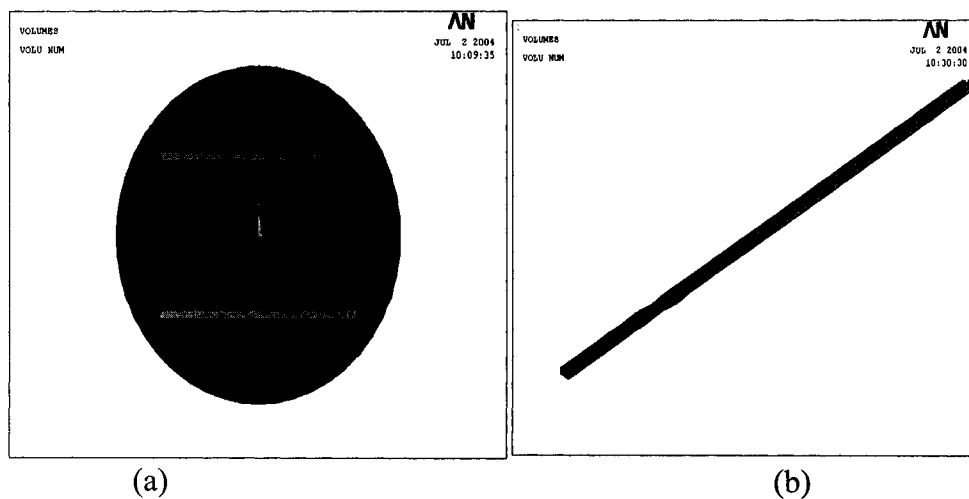


Figure 4-10 (a) A simplified cross-section of human torso. (b) The Fibre with embedded iron studs

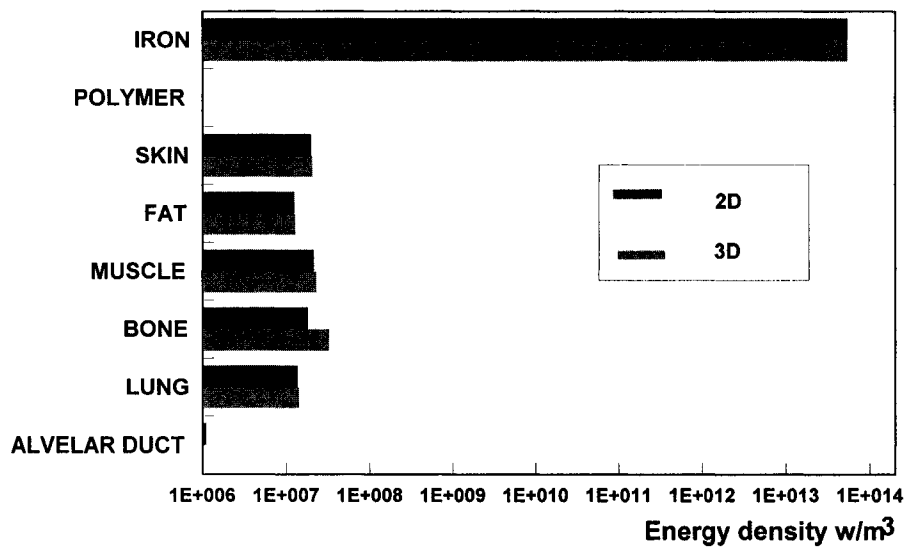


Figure 4-11 A comparison of energy density of fibre components and tissues in two models, using the same initial resistivity of $0.3 \times 10^{-5} \Omega m$ of iron. Other parameters are the same as Figure 4-6.

Figure 4-11 shows the energy density of 2-D and 3-D modeling are approximately the same. Figure 4-12 shows the final temperature of iron inside the fibre with 3-D modeling is $96^{\circ}C$. This temperature is roughly 20% higher than that in the 2-D simulation. The temperature distribution in the cross-section has a minimal difference of $0.1^{\circ}C$, less than the $0.5^{\circ}C$ in the 2-D simulation. This verifies our second assumptions in the previous solid thermal simulation.

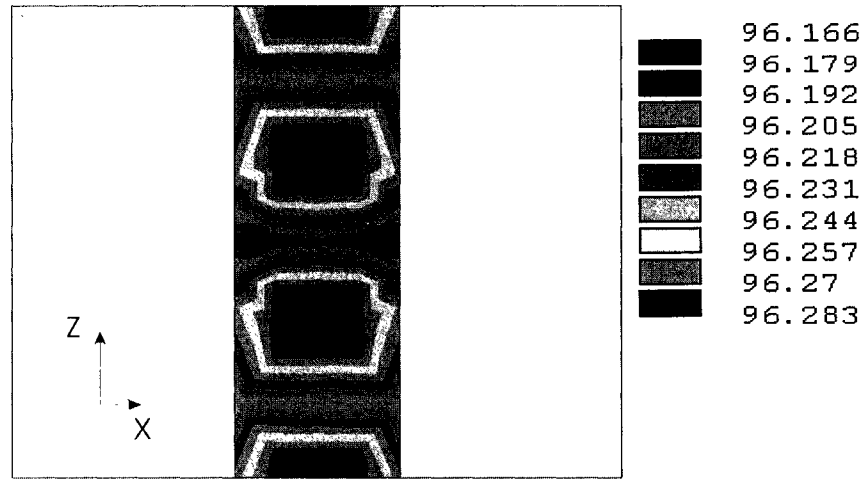


Figure 4-12 Temperature distributing in the 3-D simulation. Iron resistivity is fixed at $0.32 \times 10^{-5} \Omega\text{m}$.

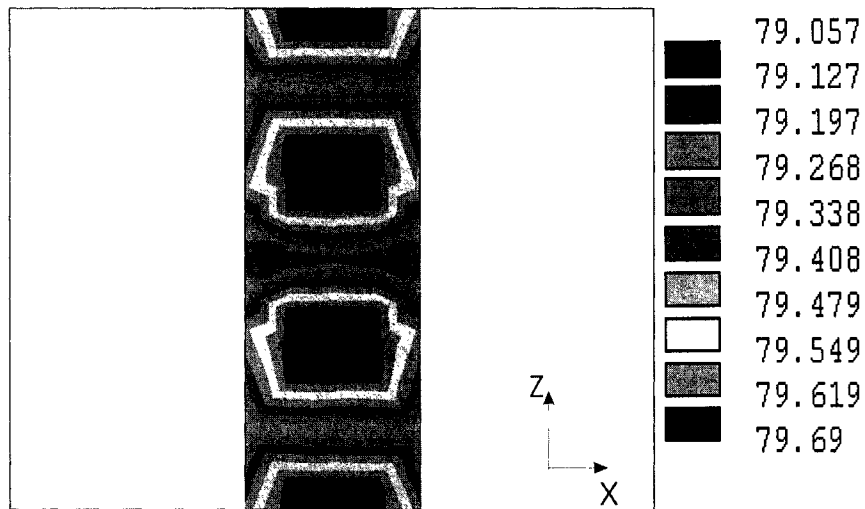


Figure 4-13 Temperature distributing in the 3-D simulation. Iron resistivity is fixed at $0.43 \times 10^{-5} \Omega\text{m}$.

The difference in the final temperature can be explained by the fixed electrical resistivity in the 3-D simulation and the nonlinear temperature dependent resistivity in the 2-D simulation. By adaptation a higher resistivity of $0.43 \times 10^{-5} \Omega\text{m}$, the simulation gives a temperature rising shown in Figure 4-13. A resistivity of 0.32×10^{-5}

Ω_m is corresponding to the starting resistivity in a 2-D simulation, while 0.43×10^{-5} Ω_m is almost equal to the resistivity of 80°C (refer to Figure 3-6). By theory, the thermal dissipation rate is linearly proportional to electrical conductivity. By fixing the resistivity in the 2-D model, we achieve almost the same energy dissipation rate (Figure 4-11). By adaptation an resistivity the same as that of 80°C in 2-D model, we get approximately the same temperature distribution (Figure 4-13). These results show the energy dissipation is independent of 2-D or 3-D modeling and the validity of our assumption on temperature distribution in the longitudinal direction of 2-D model.

The physical properties of air in 2-D and 3-D simulation are those of dry air with an estimation of 0.61 in thermal conductivity and 1.026 (kJ/kg.K) of specific heat capacity. Parametric studies, combinations of thermal conductivity up to 20 and specific heat capacity up to 4000 (kJ/kg.K), show a fibre final temperature variation of less than 0.5°C , comparing to that of dry air. The distribution of temperature of air surrounding the fibre of the above situation is also almost unchanged.

Chapter 5

Parametric Study

The induced temperature rise in the fibre is a function of material property, frequency, magnetic flux density and time.

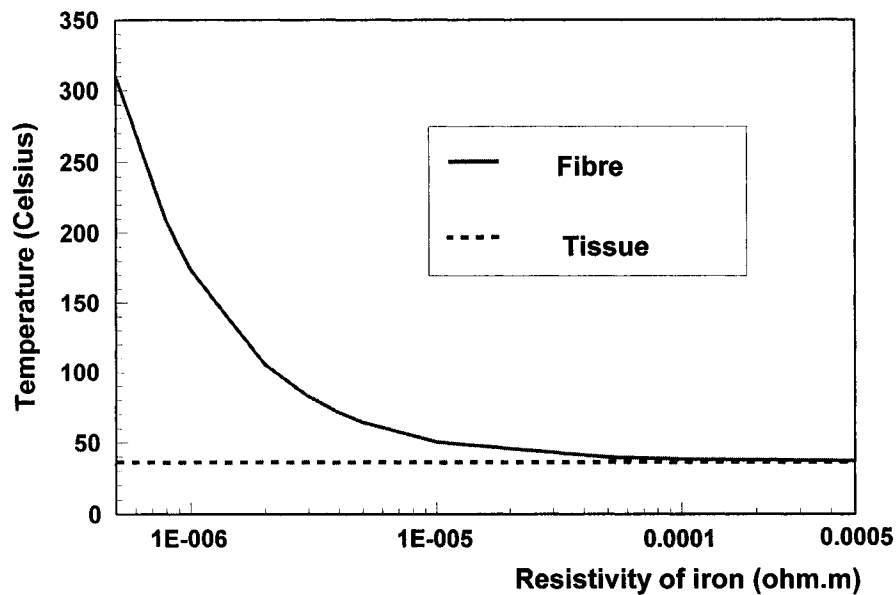


Figure 5-1. The fibre temperature as a function of iron resistivity magnetic field flux intensity 2.6kA/m, frequency 1.0 MHz. Heating time is 0.002 seconds.

Equation 2-26 shows the energy dissipation rate is inversely proportional to the electrical resistivity. Figure 5-1 shows the temperature rise of the fibre as a function of different resistivity of iron after 0.002 seconds. Here, we assume the resistivity of iron is temperature independent. The model shows that embedded iron will allow an electrical resistivity up to $10^{-5}\Omega m$ while keeping a differential temperature rise pattern.

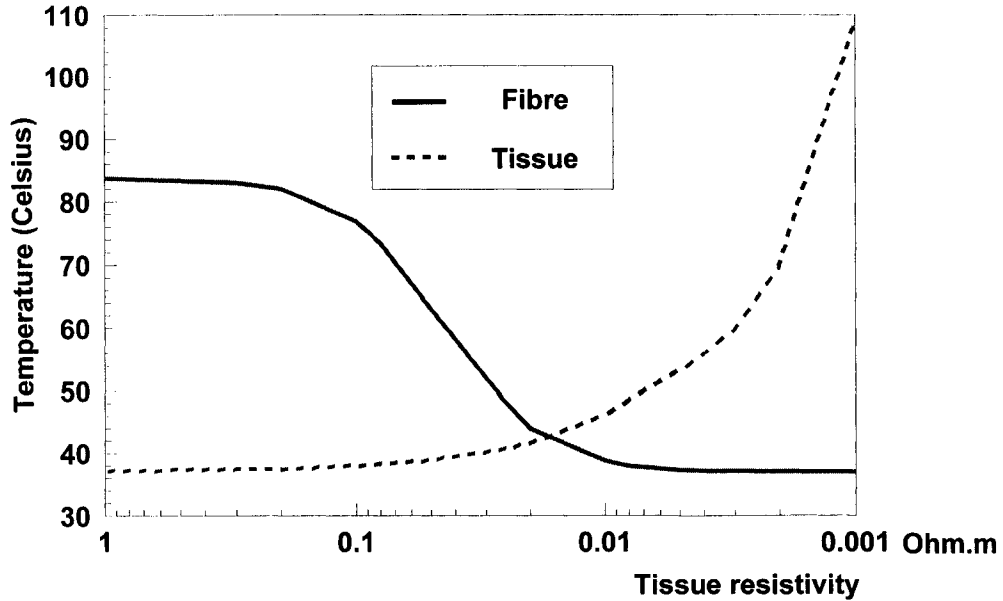


Figure 5-2. The temperature of fibre and tissue as the resistivity of the tissue changes, with other parameters as in Figure 5-1.

Figure 5-2 shows the skin tissues temperature curve as a function of its resistivity. The curve shows that as the tissue resistivity decreases, the human tissue will absorb more of the magnetic field energy. The resistivity of human tissue will decrease as the magnetic field frequency rises [7]. However, Gabriel also reported that up to MHz, of all the human tissues, eye cells show the lowest resistivity ($0.9\Omega\text{m}$); while for frequencies range up to the GHz, the lowest human tissue resistivity will be higher than $0.3\Omega\text{m}$. Figure 5-3 shows that the temperature rise in the iron is nearly linear with frequency in the 0.5-3.0MHz ranges, while the overall rise in the temperature of the tissue is less than 1.0°C . The temperature rise pattern can differ significantly for different nonlinear temperature dependant iron resistivity curves. Nevertheless, the highest temperature rise of tissue is still in the range of safety. Figure 5-4 shows the

tip displacement of the fibre as a function of temperature, which is predicted by equation (8).

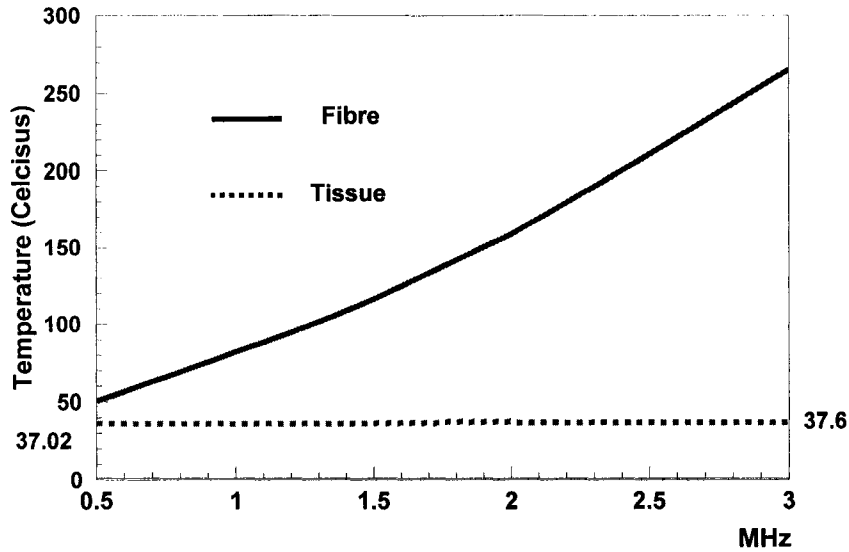


Figure 5-3. The temperature of iron fibre and tissue with respect to different frequency. The other parameters are the same as that of Figure 5-1.

Table 5-1 Energy deposition at different settings:

	1	2	3	4	5	6	7	8
H (kA/m)	26	5.2	2.6	2.6	5.2	2.6	1.3	0.43
f (MHz)	0.1	0.5	1	2	1	20	40	6
W/m ³	8.43E+13	8.43E+13	8.43E+13	3.37E+14	3.37E+14	3.37E+14	3.37E+14	8.30E+13

Table 5-1 shows energy deposition at different frequencies and magnetic flux intensities. Results shows the energy deposition rate relations of $p \sim (f \cdot H)^2$. This is predicted by equation 2-26.

The above parametric study demonstrates the validity of the model with respect to

different frequency settings and resistivity allowances. The simulation applied a value of $H.f = 2.6 * 10^9 A/m$. From equation 2-34, the frequency and the magnetic flux intensity are both second order proportional to the energy deposition rate. As a contrast, the hysteresis and Néel losses are both magnetic flux intensity second order and frequency first order dependent. Thus to achieve the same level of energy deposition rate as that of eddy current, the hysteresis and Néel relaxation losses require a higher magnetic flux intensity than seen here.

Nanotechnology can manipulate material at the nanoscale, typically having dimensions up to 100nm. The technologies for building a physical model are also available. Molecular beam epitaxial (MBE) iron can be grown on substrate with thickness from 2.5 to 30 nm [63]. MRI (Magnetic Resonance Imaging) technology can achieve a field density of a dozen Tesla at a frequency range of 1~100Mhz, scanning in the order of 1~2 milliseconds.

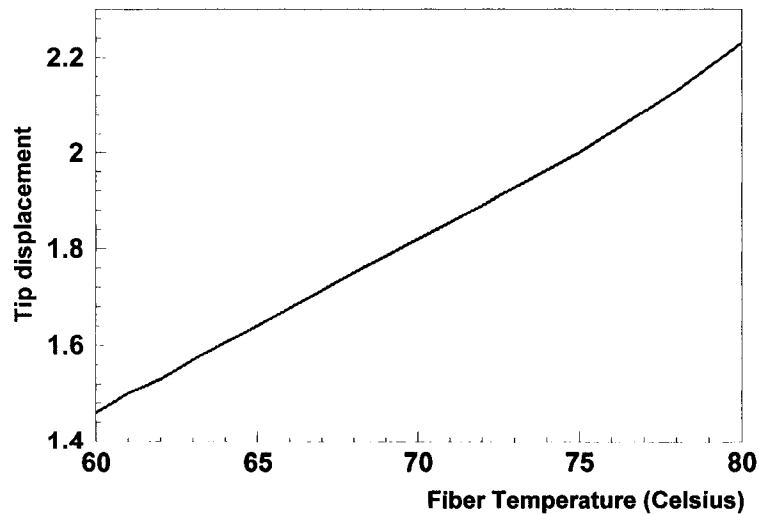


Figure 5-4. The tip displacement (μm) of the fibre as a function to temperature. The other parameters are the same as that of Figure 5-1

There are still a few questions to answer for this study, e.g., what are the smallest particle size, highest frequency and highest magnetic field intensity that eddy current works the way predicted by equation 2-26?

The author of the thesis cannot find literature on the lower limits of the particle size where eddy current theory is still valid. However, Hamad-schifferli linked DNA and protein with a 1.4 nm gold particle. By exciting eddy currents in the latter through a 1GHz magnetic field, he succeeded in dehybridizing the DNA in a manner that is localized and reversible [28]. Particle approaching this size is within the limit that hysteresis losses diminish and relaxation losses of Néel and Brownian dominate. This give us ideas on limit of smallest particle size.

The author also can not find literature about the upper frequency limit where eddy current losses are second order both frequency and magnetic field intensity proportional. The available literature [52] confirms the validities when the frequency is within several hundred Hz. However, the studies on up to MHz range is equivocal and ambiguous even it gave the approximation equation as in this study[45, 79].

Chapter 6

Conclusion and Future Work

Current interest in building fibres with microstructure results from their potential application in various area such as materials and biomedical sciences, energy storage and electrochemistry. This is the first attempt to model fibre deformation in the human lungs induced by an oscillating high frequency magnetic field.

The results from the modeling demonstrate that a high frequency magnetic field can cause thermal deformation of a fibre inside a human lung. Magnetic field flux intensity, frequency and material resistivity are the main determinants of the energy dissipation rate. The difference in electrical resistivity between iron and human tissue is the main reason for the difference in energy deposition between the two. The model is valid for frequencies between 0.5~3MHz, where the human tissue shows a minimal temperature rise since human tissues have a comparably high resistivity in this frequency range. In particular, a much lower magnetic field intensity in the model compared to those in the literature on hyperthermia[24, 29, 80] can be utilized to successfully deform a fibre, making this approach suitable for special absorption rate critical situations.

Overall, this is a 2-D nodal based model with nonlinear material properties. A 3-D edge-based model could incorporate the nonlinear material property and would give more accurate predictions of the magnetic flux distribution.

Traditional hyperthermia use ferromagnetic oxide particles in the form of either single domain or superparamagnetic materials. Synthetic nanomaterials, available in the form of magnetic fluids, have already found many interesting applications. Due to the high coercivity of the large particles, only a small portion of the hysteresis loop can be utilized in clinical application. This leads hysteresis losses are less than that of the Néel & Brownian relaxation, in vitro. Theoretically prediction of energy deposition level of Néel & Brownian relaxation losses are around $1 \times 10^{10} W / m^3$ or 2000W/g (magnetite). FEM simulation in this study numerically predicts an energy density of $1 \times 10^{13} W / m^3$. The results show that metal particles can be a good candidate in hyperthermia related applications. The results from the simulation shows that iron particles can achieve several orders higher energy density than that of the accepted peak hysteresis and Néel relaxation losses with a much lower $f \cdot H$ input. Especially, other metal particles, e.g., gold, which has a lower resistivity than iron, have a higher heating potential.

A practical experimental model could be explored by adaptation of existing MBE and MRI technologies to obtain experimental confirmation of the results. The key issue of the experiment is to verify the energy dissipation capacity of ferro conductors with respect to particle electrical conductivity, magnetic flux intensity and frequency. I would suggest starting simple model with reference to Figure 1-5 since the structure and particle size distribution can be accurately measured.

Bibliography:

1. J. Blitz, M.S., A. Inst. P., *Fundamentals of ultrasonics*. 1963, London: Butterworths.
2. Fay, P., *Introduction*, in *The RF and Microwave Handbook*, B.R. Mike Golio, Editor. 2001, CRC Press LLC, 2001.
3. Nicholas E. Buris, M.S., W. R. Deal, Vesna Radisic, Y. Qian, T. Itoh, Wayne E. Stark, Alfie Riddle, Mike Golio, K.F. Etzold, Mike Harris, *Underlying Physics*, in *The RF and Microwave Handbook*, B.R. Mike Golio, Editor. 2001, CRC Press LLC.
4. Ang, L.K. *Optimum energy absorption of a short-pulse laser in a doped dielectric slab*. in *The 2nd International Symposium on Laser Precision Microfabrication*. May 16-18 2002. Singapore.
5. CeramOptec®, *Comparative study on the use of DIODE lasers and Nd:YAG lasers for medical applications*, in *Laser- and Medicine Technology*. 1995: Berlin, Germany.
6. Hale, Q., *Applied Optical*, 1973. **12**(555).
7. Gamelia Gabriel, S.G., *Compilation of the dielectric properties of body tissues at RF and microwave frequencies*, in *Brooks Air Force Technical Report*. 1996, King's College London: London, UK.
8. Habash, R.W.Y., *Electromagnetic fields and radiation*: Marcel Dekker.
9. Foster, K.R., *Electromagnetic Field Effects and Mechanisms*. IEEE Engineering in Medicine and Biology microwave theory and techniques, 1996. **15**: p. 50-6.
10. Adey, W.R., *Biological Effects of Radio frequency electromagnetic Radiation*, in *Electromagnetic Interaction with Biological Systems*, J.C. Lin, Editor. 1989.
11. Reilly, J.P., *Peripheral Nerve Simulation by Induced Electric Currents: Exposure to Time-Varying Magnetic Fields*. Medical and Biological Engineering and Computing, 1989. **3**: p. 101-109.
12. Lai, H., *Research on the Neurological Effects of Nonionizing Radiation at the University of Washion*. Bioelectromagnetics, 1992. **13**: p. 513-26.
13. Broklehurst, B., and K.A. McLauchlan, *Free Radical Mechanism for the Effects of Environmental Electromagnetic Fields on Biological Systems*. International Journal of Radiation Biology, 1996. **69**: p. 3-24.
14. Verschaeve, L., A. Maes, *Genetic, Carcinogenic and Teratogenic Effects of Radiofrequency Fields*. Mutation Research, 1998. **410**: p. 141-165.
15. Brusick, D., R. Albertini, D. McRee, D. Peterson, G. Williams, P. Hanawalt, J. Preston, *Genotoxicity of Radiofrequency Radiation*. Environmental and Molecular Mutagenesis, 1998. **32**: p. 1-16.

16. Litoviz, T.A., D. Krause, J.M. Mullins, *Effect of Coherence Time of the Applied Magnetic Field on Ornithin Decarboxylase Activity*. Biochemical and Biophysical Research Communication, 1991. **178**: p. 862-5.
17. Graham, C., M.R. Cook, A. Sastre, D.W. Riffle, M. Gerkovich,, *Multi-Night Exposure to 60 Hz Magnetic Fields: Effects on Melatonin and its Enzymatic Metabolite*. Journal of Pineal Research, 2000. **28**: p. 1-8.
18. Q A Pankhurst, J.C., S K Jones and J Dobson, *Applications of magnetic nanoparticles in biomedicine*. J. Phys. D: Appl. Phys., 2003. **36**(2003): p. R167-R181.
19. Atkinson W J, B.I.A.a.C.D.P., *Usable frequencies in hyperthermia with thermal seeds*. IEEE Trans. Biomed. Eng. BME, 1984. **31**: p. 70-5.
20. R.Hergt, R.H., I. Hilger, W.A. Kaiser, Y. Lapatnikov, S. Margel, U. Richter, *Maghemite nanoparticles with very high AC-losses for application in RF-magnetic hyperthermia*. J. Magn. Magn. Mater., 2004. **270**(2004): p. 345-357.
21. B., L., *In Situ Activation on Microencapsulated Drugs*, Johnson Space Center: Houston, Texas.
22. Catherine C Berry, A.S.G.C., *Functionalisation of magnetic nanoparticles for application in biomedicine*. J. Phys. D: Appl. Phys., 2003. **36** (2003): p. R198-R206.
23. Ivo Safarik, M.S., *Magnetic Nanoparticles and Biosciences*. Monatshefte fur Chemie Chemical Monthly, 2002. **133**(2002): p. 737-759.
24. Gilchrist R K, M.R., Shorey W D, Hanselman R C, Parrott J C and Taylor C B, *Selective heating of lymph nodes*. Ann. Surg., 1957(146): p. 696-606.
25. Gordon RT, H.J., Gordon D, Med. Hypotheses, 1979. **5**: p. 83.
26. A. Jordan, R.S., P.Wust, H. Fahling & R. Felix, *Cancer treatment with AC magnetic field induced excitation of biocompatible superparamagnetic nanoparticles*. J. Magn. Magn. Mater., 1999. **201**: p. 413-419.
27. A.A. Kuznestsov, O.A.S., N.A. Brusentsov, O.A. Kuznetsov, *"smart" mediators for self-controlled inductive heating*. European Cells and Materials, 2002. **3 Suppl.**: p. 75-77.
28. Kimberly Hamad-schifferli, J.J.S., Aaron T. Santos, Shuguang Zhang, Joseph M. Jacobson, *Remote electronic control of DNA hybridization through inductive coupling to an attached metal nanocrystal antenna*. Natural, 2002. **415**(Jan. 2002): p. 152-155.
29. A. Jordan, P.W., H. Fahling, Int. J. Hyperthermia, 1999. **194**: p. 51.
30. Andreas Jordan, R.S., Klaus Maier-Hauff, Manfred Johannsen, Peter Wust, Jacek Nadobny, Hermann Schirra, Helmut Schmidt, Serdat Deger, Stefen Loening, Wolfgang Lanksch, Roland Felix, *Presentation of a new magnetic field therapy system for the treatment of human solid tumors*

- with magnetic fluid hyperthermia*. Journal of Magnetism and Magnetic Materials, 2001. **225**(2001): p. 118-126.
31. Stereotaxis, I., <http://www.stereotaxis.com>. 2002.
 32. FeRx, I., <http://www.ferx.com/>. 2004.
 33. Ingrid Hilger, K.F., Wilfried Andra, Robert Hiergeist, Rudolf Hergt, Werner A. Kaiser, *Heating Potential of Iron Oxides for Therapeutic Purposes in Interventional Radiology*. Acad Radiol 2002, Aug,2002. **9**: p. 198-202.
 34. Leach, J.H., *Magnetic Target Drug Delivery*, in *Electrical Engineering*. 2003, Virginia Polytechnic Institute and State University.
 35. Gareth P. Hatch, R.E.S., *Magnetic design considerations for devices and particles used for biological high-gradient magnetic separation (HGMS) systems*. Journal of Magnetism and Magnetic Materials, 2001. **225**(2001): p. 262-276.
 36. J. L. Snoek, Physica A, 1948. **15**(207).
 37. Igor T. Iakubov, A.N.L., Sergei A. Maklakov, Alexei V. Osipov, Konstantin N. Rozanov, Ilya A. Ryzhikov, Nikolai A. Simonov, Sergei N. Starstenko, *Experimental study of microwave permeability of Fe thin films*. Journal of Magnetism and Magnetic Materials, 2003. **258-259**: p. 195-197.
 38. Y. M. Kim, D.C., K.H. Kim, J.Kim, S. H. Han, H. J. Kim, *Thickness effects on the high-frequency characteristics of as-deposited Co-Ni-Fe and Co-Ni-Fe-N soft magnetic thin films*. J. Magn. Mater., 2002. **239**(2002): p. 498-501.
 39. Takaomi Itoi, A.I., *High-frequency permeability of (Fe, Co, Ni)₆₂Nb₈B₃₀ amorphous alloys with a wide supercooled liquid region*. Applied Physics Letter, 1999. **76**(17): p. 2510-2512.
 40. K. H. Kim, J.H.J., J. Kim, S.H. Han, H. J. Kim, *High moment and high frequency permeability Fe-B-N nanocrystalline soft magnetic films*. Journal of Magnetism and Magnetic Materials, 2002. **239**(200): p. 487-489.
 41. Sharrock, M.P., IEEE Trans. Mag., 1990. **26**(1990): p. 193.
 42. R.E.Rosensweig, *Heating magnetic fluid with alternating magnetic field*. Journal of Magnetism and Magnetic Materials, 2002. **252**(2002): p. 370-374.
 43. Rudolf Hergt, W.A., Carl G. d'Ambly, Ingrid Hilger, Werner A. Kaiser, Uwe Richter, and Hans-George Schmidt, *Physical Limits of Hyperthermia Using Magnetite Fine Particles*. IEEE Transactions on magnetics, 1998. **34**(5).
 44. Toshifumi Schimizu, M.M., *New magnetic implant material for interstitial hyperthermia*. Science and technology of advanced materials, 2003. **4**(2003): p. 469-473.

45. K.W.E. Cheng, W.S.L., C.Y. Tang, L.C. Chan, *Dynamic modelling of magnetic materials for high frequency applications*. Journal of Magnetism and Magnetic Materials, 2003. **139**(2003): p. 578-584.
46. Ming Ma, Y.W., Jie Zhou, Yongkang Sun, Yu Zhang, Ning Gu, *Size dependence of specific power absorption of Fe₃O₄ particles in AC magnetic field*. J. Magn. Magn. Mater., 2004. **268**(2004): p. 33-39.
47. Chikazumi, S., *Physics of Magnetism*. 1964, PA.: Lippincott.
48. L. D. Laudan, E.M.L., *Electrodynamics of Continuous Media*. 1960, London, U.K.: Pergamo.
49. John Davies, P.S., *Induction Heating Handbook*. 1979: McMRA W-HILL Book Company (UK) Limited.
50. Causer, W., *Effective permeability and iron loss in sheets and wires with weak magnetic fields*. Arch. Elektrotech. **15**: p. 308-19.
51. Yueqiang Liu, A.B., R. Bergstrom, M. G. Larson, K. Samuelsson, *Edge Element Computations of Eddy Currents in Laminated Materials*. IEEE Trans. on magnetics, 2003. **39**(May, 2003): p. 1758-1765.
52. Bozorth, R.M., *Ferromagnetism*. 1959.
53. J.F. Cochran, B.H., and A.S. Arrott, *Ferromagnetic resonance in a system composed of a ferromagnetic substrate and an exchange-coupled thin ferromagnetic overlayer*. Physical review B, 1986. **34**(11): p. 7788-7801.
54. J.G. Zhu, S.Y.R.H., B.V.S. Ramsden, *Discrete, modelling of magnetic cores including hysteresis eddy current and anomalous losses*. IEEE Proc. A, 1993. **140** 4)(1993): p. 317-322.
55. Y.H. Shang, W.F., W. Moussa. *Thermally induced fiber deformation using high frequency magnetic field*. in ICMENS2004. 2004. Banff, Canada.
56. ANSYS, *ANSYS Multiphysics 8.0*. 2004.
57. John H. Lienhard IV, J.H.L.V., *A Heat transfer Textbook*. 2003.
58. Mikron, *Table of emission of various surfaces*. 2000, Mikron Instrument Company, Inc. p. 4.
59. M.W. Judy, Y.-H.C., R.T. Howe, A.P. Pisano, *Self-adjusting microstructure (SAMS)*. IEEE, 1991.
60. Timshenko, S., *Analysis of bi-metal thermostats*. Journal of the Optical Society of America, 1925. **11**: p. 233-55.
61. B. Edmon, J., J. Ernstberger, K. Ghosh, J. Malaugh, D. Nofodjo, W. Samyono, X. Xu, D. Dausch, S. Goodwin, R.C. Smith, *Electrostatic Operation and Curvature Modeling for a MEMS Flexible Film Actuator*. 2004, Statics and Applied Mathematical Sciences Institute.
62. State, G., *Ferromagnetic Curie Temperature*: Georgia State University.
63. R. Pulwey, M.Z., G. Bayreuther, and D. Weiss, *Transition of magnetocrystalline anisotropy and domain structure in epitaxial Fe(001) nanomagnets*. Journal of Applied Physics, 2003. **93**(10): p. 7432-7434.

64. C.M.Gurtler, Y.B.X., J.A.C. Bland, *In Situ study of the temperature-dependent magnetoresistance of ultrathin epitaxial Fe films on GaAs(100)*. J. Magn. Magn. Mater., 2001. **226-230**(2001): p. 655-657.
65. D. Jaccard, A.T.H., G. Behr, Y. Inada, Y. Onuki, *Superconductivity of gamma-Fe: complete resistive transition*. Physics Letters A, 2001. **299**(2002): p. 282-286.
66. K. Pekala, M.P., *Low temperature transport properties of nanocrystalline Cu, Fe and Ni*. Nanostructure Materials, 1995. **6**(1995): p. 819-822.
67. Shackelford, J.F.e.a., in *Materials science and engineering handbook*, E.J.F.S.W. Alexander, Editor. 2001, Boca Raton: CRC Press LLC, 2001.
68. Dugdale, J.S., *The electrical Properties of Metals and Alloys*. 1977, London: Edward Arnold Ltd.
69. K.G. Suresh, K.V.S.R.R., *Electrical resistivity studies on ((Er(1-x)Pr(x))(2)Fe(17))*. Journal of Alloys and Compounds, 1996. **238**(1996): p. 90-94.
70. Mannari, I., Progr. Theor. Phys., **22**(1959): p. 335.
71. Kasuya, T., Progr. Theor. Phys., 1959. **22**(1959): p. 227.
72. N.V. Volkenstein, V.P.D., V.E. Startsev, Progr. Theor. Phys., 1973. **57**(1973): p. 9.
73. A. Kowalczyzysk, G.C., V. Ivanov, J. Baszynski, J. Magn. Magn. Mater., 1995. **139**(1995): p. 19.
74. E. Gratz, H.R.K., J. Magn. Magn. Mater. **2**(1976): p. 187.
75. E. Gratz, M.J.Z., *Handbook on Physics and Chemistry of Rare Earths*, ed. L. Eyring. 1982, North-Holland, Amsterdam. Chapter 42. P. 117.
76. X.X. Zhang, H.L., K.K. Fung, B.X. Qin, *Electrical transport properties in the passivated magnetic small iron particles*. Physica B, 2000. **279**(2000): p. 185-187.
77. J. Barton Hoag, H.J., *Permeability of Ultra-Radio Frequencies*. Physical review, 1932. **42**: p. 571-5.
78. Wait, G.R., Phys. Rev., 1927. **29**: p. 566.
79. Thompson, M.T., *SDimple Models and Measurements of Magnetically Induced Heating Effects in Ferromagnetic Fluids*. IEEE Transaction on magnetics, 1998. **34**(5): p. 3755-3764.
80. Gilchrist R K, S.W.D., Hanselman R C, Depeyster F A, Yang J, Medal R, Ann. Surg., 1965. **79**: p. 427-431.